The Astrophysical Journal, 716:712–738, 2010 June 10 doi:10.1088/0004-637X/716/1/712

SPECTRA AND *HUBBLE SPACE TELESCOPE* LIGHT CURVES OF SIX TYPE Ia SUPERNOVAE AT $0.511 < z < 1.12$ AND THE UNION2 COMPILATION*

R. Amanullah[1,2], C. Lidman[2], D. Rubin[3,4], G. Aldering[3], P. Astier[5], K. Barbary[3,4], M. S. Burns[6], A. Conley[7], K. S. Dawson[8], S. E. Deustua[9], M. Doi[10], S. Fabbro[11], L. Faccioli[3,12], H. K. Fakhouri[3,4], G. Folatelli[13], A. S. Fruchter[9], H. Furusawa[14], G. Garavini[1], G. Goldhaber[3,4], A. Goobar[1,2], D. E. Groom[3], I. Hook[15,16], D. A. Howell[17,18], N. Kashikawa[14], A. G. Kim[3], R. A. Knop[19,27], M. Kowalski[20], E. Linder[12], J. Meyers[3,4], T. Morokuma[14,28], S. Nobili[1,2], J. Nordin[1,2], P. E. Nugent[3], L. Östman[1,2], R. Pain[5], N. Panagia[9,21,22], S. Perlmutter[3,4], J. Raux[5], P. Ruiz-Lapuente[23], A. L. Spadafora[3], M. Strovink[3,4], N. Suzuki[3], L. Wang[24], W. M. Wood-Vasey[25], and N. Yasuda[26]
(The Supernova Cosmology Project)
[1] Department of Physics, Stockholm University, Albanova University Center, SE-106 91 Stockholm, Sweden
[2] The Oskar Klein Centre for Cosmoparticle Physics, Department of Physics, AlbaNova, Stockholm University, SE-106 91 Stockholm, Sweden
[3] E. O. Lawrence Berkeley National Laboratory, 1 Cyclotron Road, Berkeley, CA 94720, USA
[4] Department of Physics, University of California Berkeley, Berkeley, CA 94720-7300, USA
[5] LPNHE, Université Pierre et Marie Curie Paris 6, Université Paris Diderot Paris 7, CNRS-IN2P3, 4 place Jussieu, 75005 Paris, France
[6] Colorado College, 14 East Cache La Poudre Street, Colorado Springs, CO 80903, USA
[7] Center for Astrophysics and Space Astronomy, University of Colorado, 389 UCB, Boulder, CO 80309, USA
[8] Department of Physics and Astronomy, University of Utah, Salt Lake City, UT 84112, USA
[9] Space Telescope Science Institute, 3700 San Martin Drive, Baltimore, MD 21218, USA
[10] Institute of Astronomy, School of Science, University of Tokyo, Mitaka, Tokyo, 181-0015, Japan
[11] Department of Physics and Astronomy, University of Victoria, P.O. Box 3055, Victoria, BC V8W 3P6, Canada
[12] Space Sciences Laboratory, University of California Berkeley, Berkeley, CA 94720, USA
[13] Observatories of the Carnegie Institution of Washington, 813 Santa Barbara Street, Pasadena, CA 9110, USA
[14] National Astronomical Observatory of Japan, 2-21-1 Osawa, Mitaka, Tokyo 181-8588, Japan
[15] Sub-Department of Astrophysics, University of Oxford, Denys Wilkinson Building, Keble Road, Oxford OX1 3RH, UK
[16] INAF-Osservatorio Astronomico di Roma, via Frascati 33, 00040 Monteporzio (RM), Italy
[17] Las Cumbres Observatory Global Telescope Network, 6740 Cortona Drive, Suite 102, Goleta, CA 93117, USA
[18] Department of Physics, University of California, Santa Barbara, Broida Hall, Mail Code 9530, Santa Barbara, CA 93106-9530, USA
[19] Meta-Institute of Computational Astronomy
[20] Physikalisches Institut, Universität Bonn, Nussallee 12, D-53115 Bonn, Germany
[21] INAF-Osservatorio Astrofisico di Catania, Via Santa Sofia 78, I-95123, Catania, Italy
[22] Supernova Ltd., OYV #131, Northsound Road, Virgin Gorda, British Virgin Islands
[23] Department of Astronomy, University of Barcelona, Barcelona, Spain
[24] Department of Physics, Texas A&M University, College Station, TX 77843, USA
[25] Department of Physics and Astronomy, 3941 O'Hara Street, University of Pittsburgh, Pittsburgh, PA 15260, USA
[26] Institute for Cosmic Ray Research, University of Tokyo, Kashiwa 277 8582, Japan
Received 2009 December 7; accepted 2010 April 11; published 2010 May 21

ABSTRACT

We report on work to increase the number of well-measured Type Ia supernovae (SNe Ia) at high redshifts. Light curves, including high signal-to-noise *Hubble Space Telescope* data, and spectra of six SNe Ia that were discovered during 2001, are presented. Additionally, for the two SNe with $z > 1$, we present ground-based *J*-band photometry from Gemini and the Very Large Telescope. These are among the most distant SNe Ia for which ground-based near-IR observations have been obtained. We add these six SNe Ia together with other data sets that have recently become available in the literature to the Union compilation. We have made a number of refinements to the Union analysis chain, the most important ones being the refitting of all light curves with the SALT2 fitter and an improved handling of systematic errors. We call this new compilation, consisting of 557 SNe, the Union2 compilation. The flat concordance ΛCDM model remains an excellent fit to the Union2 data with the best-fit constant equation-of-state parameter $w = -0.997^{+0.050}_{-0.054}(\mathrm{stat})^{+0.077}_{-0.082}(\mathrm{stat + sys\ together})$ for a flat universe, or $w = -1.038^{+0.056}_{-0.059}(\mathrm{stat})^{+0.093}_{-0.097}(\mathrm{stat + sys\ together})$ with curvature. We also present improved constraints on $w(z)$. While no significant change in w with redshift is detected, there is still considerable room for evolution in w. The strength of the constraints depends strongly on redshift. In particular, at $z \gtrsim 1$, the existence and nature of dark energy are only weakly constrained by the data.

Key words: cosmological parameters – cosmology: observations – supernovae: general

Online-only material: color figures, machine-readable tables

* Based in part on observations made with the NASA/ESA *Hubble Space Telescope*, obtained from the data archive at the Space Telescope Science Institute (STScI). STScI is operated by the Association of Universities for Research in Astronomy (AURA), Inc. under the NASA contract NAS 5-26555. The observations are associated with programs HST-GO-08585 and HST-GO-09075. Based, in part, on observations obtained at the ESO La Silla Paranal Observatory (ESO programs 67.A-0361 and 169.A-0382). Based, in part, on observations obtained at the Cerro-Tololo Inter-American Observatory (CTIO), National Optical Astronomy Observatory (NOAO). Based on observations obtained at the Canada–France–Hawaii Telescope (CFHT). Based, in part, on observations obtained at the Gemini Observatory (Gemini programs GN-2001A-SV-19 and GN-2002A-Q-31). Based, in part on observations obtained at the Subaru Telescope. Based, in part, on data that were obtained at the W. M. Keck Observatory.

[27] http://www.physics.drexel.edu/mica

[28] Research Fellow of the Japan Society for the Promotion of Science.

1. INTRODUCTION

Type Ia supernovae (SNe Ia) are an excellent tool for probing the expansion history of the universe. About a decade ago, combined observations of nearby and distant SNe Ia led to the discovery of the accelerating universe (Perlmutter et al. 1998, 1999; Garnavich et al. 1998; Schmidt et al. 1998; Riess et al. 1998).

Following these pioneering efforts, the combined work of several different teams during the past decade has provided an impressive increase in both the total number of SNe Ia and the quality of the individual measurements. At the high redshift end ($z \gtrsim 1$), the *Hubble Space Telescope* (*HST*) has played a key role. It has successfully been used for high-precision optical and infrared follow-up of SNe discovered from the ground (Knop et al. 2003; Tonry et al. 2003; Barris et al. 2004; Nobili et al. 2009), and, by using the Advanced Camera for Surveys (ACS), to carry out both search and follow-up from space (Riess et al. 2004, 2007; Kuznetsova et al. 2008; Dawson et al. 2009). At the same time, several large-scale ground-based projects have been populating the Hubble diagram at lower redshifts. The Katzman Automatic Imaging Telescope (Filippenko et al. 2001), the Nearby Supernova Factory (Copin et al. 2006), the Center for Astrophysics SN group (Hicken et al. 2009b), the Carnegie Supernova Project (Hamuy et al. 2006; Folatelli et al. 2010), and the Palomar Transient Factory (Law et al. 2009) are conducting searches and/or follow-up for SNe at low redshifts ($z < 0.1$). The SN Legacy Survey (SNLS; Astier et al. 2006) and ESSENCE (Miknaitis et al. 2007; Wood-Vasey et al. 2007) are building SN samples over the redshift interval $0.3 < z < 1.0$, and the Sloan Digital Sky Survey (SDSS) SN Survey (Holtzman et al. 2008; Kessler et al. 2009) is building an SN sample over the redshift interval $0.1 < z < 0.3$, a redshift interval that has been relatively neglected in the past. These projects have discovered ~700 well-measured SNe. The number of well-measured SNe beyond $z \sim 1$ is approximately 20 and is comparatively small.

Kowalski et al. (2008, hereafter K08) provided a framework to analyze these and future data sets in a homogeneous manner and created a compilation, called the "Union" SNe Ia compilation, of what was then the world's SN data sets. Recently, Hicken et al. (2009a, hereafter H09) added a significant number of nearby SNe to a subset of the "Union" set to create a new compilation, and similarly the SDSS SN survey (Kessler et al. 2009, hereafter KS09) carried out an analysis of a compilation including their large intermediate-z data set (Holtzman et al. 2008). When combined with baryon acoustic oscillations (Eisenstein et al. 2005), the H09 compilation leads to an estimate of the equation-of-state (EOS) parameter that is consistent with a cosmological constant, while KS09 get significantly different results depending on which light-curve fitter they use.

An important role for SNe Ia beyond $z \sim 1$, in addition to constraining the time evolution of w, is their power to constrain astrophysical effects that would systematically bias cosmological fits. Most evolutionary effects are expected to monotonically change with redshift and are not expected to mimic dark energy over the entire redshift interval over which SNe Ia can be observed. Evolutionary effects might also have additional detectable consequences, such as a shift in the average color of SNe Ia or a change in the intrinsic dispersion about the best-fit cosmology.

Interestingly, the most distant SNe Ia in the Union compilation (defined here as SNe Ia with $z \gtrsim 1.1$) are almost all redder than the average color of SNe Ia over the redshift interval $0.3 < z < 1.1$. The result is unexpected as bluer SNe Ia at lower redshifts are also brighter (Tripp 1998; Guy et al. 2005) and should therefore be easier to detect at higher redshifts. Possible explanations for the redder than average colors of very distant SNe Ia range from the technical, such as an incomplete understanding of the calibration of the instruments used for obtaining the high redshift data, to the more astrophysically interesting, such as a real lack of bluer SNe at high redshifts.

The underlying assumption in using SNe Ia in cosmology is that the luminosity of both near and distant events can be standardized with the same luminosity versus color and luminosity versus light-curve shape relationships. While drifts in SN Ia populations are expected from a combination of the preferential discovery of brighter SNe Ia and changes in the mix of galaxy types with redshift (Howell et al. 2007)—effects that will affect different surveys by differing amounts—a lack of evolution in these relationships with redshift has not been convincingly demonstrated given the precision of current data sets. This assumption needs to be continuously examined as larger and more precise SN Ia data sets become available.

In this paper, we report on work to increase the number of well-measured distant SNe Ia by presenting SNe Ia that were discovered in ground-based searches during 2001 and then followed with Wide Field Planetary Camera 2 (WFPC2) on *HST*. Two of the new SNe Ia are at $z \sim 1.1$ and have high-quality ground-based infrared observations that were obtained with ISAAC on the Very Large Telescope (VLT) and NIRI on Gemini. This paper is the first paper in a series of papers that will provide a comparable sample of $z > 1$ SNe Ia to the SNe now available in the literature. The SNe Ia in this series of papers were discovered in 2001 (this paper), 2002 (N. Suzuki et al. 2010, in preparation) and from 2005 to 2006 during the Supernova Cosmology Project (SCP) cluster survey (Dawson et al. 2009).

This paper is organized as follows. In Section 2, we describe the SN search and the spectroscopic confirmation, while Sections 3, 4, and 5 contain a description of the follow-up imaging and the SN photometry. The light-curve fitting is described in Section 6. In Section 7, we update the K08 analysis both by adding new data and by improving the analysis chain. The paper ends with a discussion and a summary.

2. SEARCH, DISCOVERY, AND SPECTROSCOPIC CONFIRMATION

The SNe were discovered during two separate high-redshift SN search campaigns that were conducted during the Northern Spring of 2001. The first campaign (hereafter Spring 2001) consisted of searches with the CFH12k (Cuillandre et al. 2000) camera on the 3.4 m Canada–France–Hawaii Telescope (CFHT) and the MOSAIC II (Muller et al. 1998) camera on the 4.0 m Cerro-Tololo Inter-American Observatory (CTIO) Blanco telescope. The second campaign (hereafter Subaru 2001) was done with SuprimeCam (Miyazaki et al. 2002) on the 8.2 m Subaru telescope. All searches were "classical" searches (Perlmutter et al. 1995, 1997), i.e., the survey region was observed twice with a delay of approximately 1 month between the two observations, and the two epochs were then analyzed to find transients. Details of the search campaigns can be found in Lidman et al. (2005) and Morokuma et al. (2010).

The Spring 2001 data were processed to find transient objects and the most promising candidates were given an internal SCP name and a priority. The priority was based on

Table 1
List of the Instruments and Telescopes Used for Spectroscopy

Search	Instr./Tel.	Detector	Resolution	Observing Dates
Spring 2001	FORS1/Antu	Tektronix 2k × 2k CCD	500	2001 April 21–22
Spring 2001	LRIS/Keck I	Tektronix 2k × 2k CCD	850	2001 April 20
Spring 2001	ESI/Keck II	MIT-LL 2k × 4k CCD	5000	2001 April 21–24
Subaru 2001	FOCAS/Subaru	SITe 2k × 4k CCD	1000	2001 May 26–27

Table 2
Summary of the Spectroscopic Observations

IAU Name	Search	α(2000)	δ(2000)	$E(B-V)$	MJD (days)	Instr./Tel.	Exp. (s)
SN 2001cw	Subaru 01	$15^h23^m06^s.3$	+29°39′32″	0.024	52056.6	FOCAS/Subaru[a]	4200
SN 2001gn	Spring 01	$14^h01^m59^s.9$	+05°05′00″	0.028	52023.1	ESI/Keck II[b]	9700
SN 2001go	Spring 01	$14^h02^m00^s.9$	+05°00′59″	0.027	52021.3	FORS1/Antu[a]	2400
SN 2001gq	Spring 01	$14^h01^m51^s.4$	+04°53′12″	0.027	52020.3	LRIS/Keck[a]	3600
SN 2001gy	Spring 01	$13^h57^m04^s.5$	+04°31′00″	0.030	52021.3	FORS1/Antu[a]	2400
SN 2001hb	Spring 01	$13^h57^m11^s.9$	+04°20′27″	0.032	52024.3	ESI/Keck II[b]	3600

Notes. For completeness, the observations that are reported in Lidman et al. (2005) and Morokuma et al. (2010) are also included. The Galactic extinction, $E(B-V)$, from Schlegel et al. (1998), is presented together with the coordinates for each SN.
[a] Long slit.
[b] Echellette.

Table 3
Classifications, Redshifts, CI (Howell et al. 2005), and Matches to Nearby SN Spectra (or Templates)

IAU Name	CI	Spectroscopic Classification		Redshift	Template Match	t_{Spec} (days)	t_{LC} (days)	Δt (days)
2001cw	3	Ia*	SF	0.95 ± 0.01	1989B	−5	−5.1 ± 0.4	+0.1
2001gn	3	Ia*	SF	1.124	1990N	−7	−3.4 ± 0.1	−3.6
2001go	5	Ia	Si II	0.552	1992A	+5	+6.5 ± 0.2	−1.5
2001gq	3	Ia*	SF	0.672	1999bp	−2	−5.1 ± 0.2	+3.1
2001gy	5	Ia	Si II	0.511	1990N	−7	−6.9 ± 0.2	−0.1
2001hb	3	Ia*	SF	1.03 ± 0.02	1989B	−7	−6.8 ± 0.5	−0.2

Notes. Unless indicated otherwise, the uncertainty in the redshift is 0.001. Here t_{Spec} shows the spectroscopic phase relative to maximum light in the B band of the template, t_{LC} shows the rest-frame phase of the observation relative to the fitted B-band maximum (MJD_{max} in Table 6), and Δt is the difference. The CI and spectroscopic classification are explained in detail in the text. We also specify whether the classification was done from the fit ("SF") or if "Si II" could be identified.

a number of factors: the significance of the detection, the relative increase in the brightness, the distance from the center of the apparent host, the brightness of the candidate, and the quality of the subtraction. Note however that these factors were not applied independently of each other, but the priorities were rather based on a combination of factors. For example, candidates on core were only avoided if they had a small relative brightness increase over the span of 1 month. The AGN structure function shows that AGNs rarely have strong changes over 1 month.

The candidates discovered in the Spring 2001 campaign were distributed to teams working at Keck and Paranal observatories for spectroscopic confirmation. The distribution was based on the likely redshifts. Candidates that were likely to be SNe Ia at $z \gtrsim 0.7$ were sent to Keck, while candidates that were thought to be nearer were sent to the VLT. In later years, when FORS2 was upgraded with a CCD with increased red sensitivity, the most distant candidates would also be sent to the VLT. All Subaru 2001 candidates were sent to FOCAS (Faint Object Camera And Spectrograph) on Subaru for spectroscopic confirmation (Morokuma et al. 2010).

In total, four instruments (FORS1 on the ESO-VLT, ESI and LRIS on Keck, and FOCAS on Subaru) were used to determine redshifts and to spectroscopically confirm the SN type. The dates of the spectroscopic runs are listed in Table 1 and the observations of individual candidates are listed in Table 2.

Only those candidates that were confirmed as SNe Ia were then scheduled for follow-up observations from the ground and with *HST*. In total, six SNe were sent for *HST* follow-up: one from the Subaru 2001 campaign and five from the Spring 2001 campaign. The SNe are listed in Tables 2 and 3. Finding charts are provided in Figure 1.

Here, we describe the analysis of data that were taken with ESI and LRIS. The analyses of the spectra taken with FORS1 and FOCAS (SN 2001cw, SN 2001go, and SN 2001gy) are described in Lidman et al. (2005) and Morokuma et al. (2010), respectively. The spectra of these SN are shown in these papers and will not be repeated here.

2.1. ESI

The two highest redshift candidates, 2001gn and 2001hb, were observed with the echelette mode of ESI (Sheinis et al. 2002). A spectrum taken with the echellette mode of ESI and the 20″ slit covers the 0.39–1.09 μm wavelength range and is spread over 10 orders ranging in dispersion from 0.16 Å pixel^{-1} in the bluest order (order 15) to 0.30 Å pixel^{-1} in the reddest (order 6). The detector is a MIT-Lincoln Labs

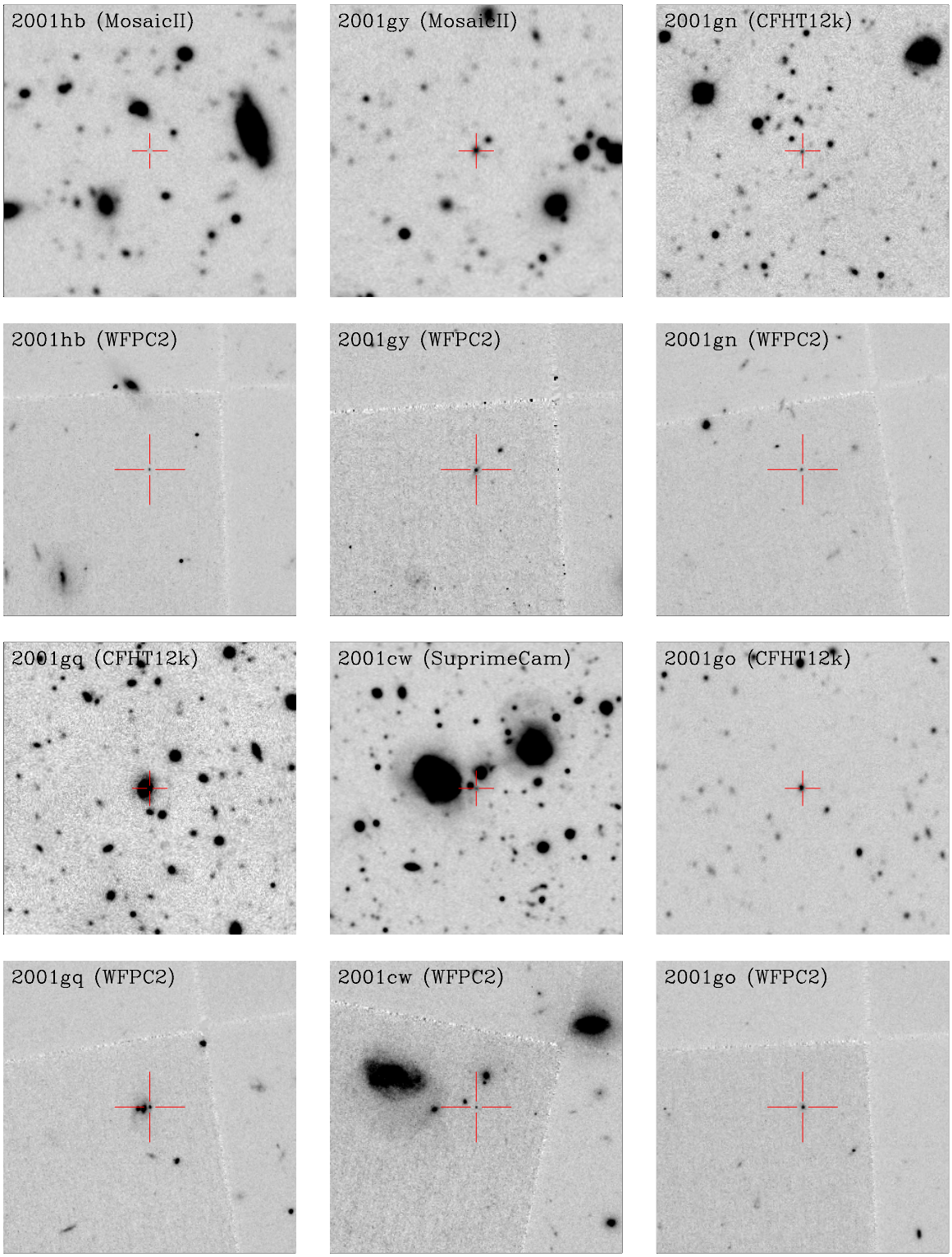

Figure 1. SN finding charts. North is up and east is to the left. The SNe are marked with red cross hairs. The images have been created by stacking all *I*-band data taken with the search instrument and all *F814W* data obtained with WFPC2. The patch widths are 1′ and 0.′5 for the ground-based and *HST* images, respectively.
(A color version of this figure is available in the online journal.)

2048 × 4096 CCD with 15 μm pixels. The slit width was set according to the seeing conditions and varied from 0.″7 to 1.″0, which corresponds to a spectral resolution of $R \sim 5000$. Compared to spectra obtained with low-resolution spectrographs, such as FORS1, FORS2, LRIS, and FOCAS, the fraction of the ESI spectrum that is free of bright night sky lines from Earth's atmosphere is much greater. This allows one to de-weight the low signal-to-noise regions that overlap these bright lines when binning the spectra, a method that becomes inefficient with low-resolution spectra as too much of the spectra are de-weighted. Another advantage of ESI was that the MIT-LL CCD offered high quantum efficiency at red wavelengths and significantly reduced fringing compared to conventional backside-illuminated CCDs.

Table 4
Instruments and Telescopes Used for Photometric Follow-up

Tel./Instr.	Scale ($''$ pixel^{-1})	FOV ($'$)	Detectors	Search
CFHT/CFH12k	0.206	42 × 28	12 MIT 2k × 4k CCD	Spring 2001
CTIO/MOSAIC II	0.27	36 × 36	8 SITe 2k × 2k CCD	Spring 2001
VLT/FORS1	0.20	6.8 × 6.8	1 Tektronix 2k × 2k CCD	Spring 2001
VLT/ISAAC	0.1484	2.5 × 2.5	Hawaii 1k × 1k HgCdTe array	Spring 2001
NTT/SuSI2	0.08	5.5 × 5.5	2 EEV 2k × 4k CCD	Spring 2001
Gemini/NIRI	0.1171	2.0 × 2.0	Aladdin 1k × 1k InSb array	Spring 2001
HST/ACS	0.05	2.4 × 2.4	2 SITe 2k × 4k CCD	Spring 2001
HST/WFPC2 (PC)	0.046	0.61 × 0.61	1 Loral Aerospace 800 × 800 CCD	Both
Subaru/SuprimeCam	0.20	34 × 27	10 MIT/LL 2k × 4k CCD	Subaru 2001

Note. For WFPC2 we only list the properties of the PC camera which was always used for targeting the SNe.

The data were reduced in a standard manner. The bias was removed by subtracting the median of the pixel values in the overscan regions, the relative gains of the two amplifiers were normalized by multiplying one of the outputs with a constant and the data were flat fielded with internal lamps. When extracting SN spectra, a bright star was used to define the trace along each order, and the spectrum of the SN was used to define the center of the aperture. Once extracted, the 10 orders were wavelength calibrated (using internal arc lamps and cross-checking the result with bright OH lines), flux calibrated, and stitched together to form a continuous spectrum.

To reduce the impact that residuals from bright OH lines have on determining the redshift and classifying the candidate, the spectrum was weighted according to the inverse square of the error spectrum and then rebinned by a factor of 20, from 0.19 Å pixel^{-1} to 3.8 Å pixel^{-1}. The binning was chosen so that features from the host were not lost.

The reduced spectra of 2001gn and 2001hb are presented in Figures A1 and A2, respectively.

2.2. LRIS

The LRIS (Oke et al. 1995) data were taken with the 400/8500 grating and the GG495 order sorting filter and were reduced in a standard manner. The bias was removed with a bias frame, the pixel-to-pixel variations were normalized with flats that were taken with internal lamps, and the background was subtracted by fitting a low-order polynomial along detector columns. The fringes that were not removed by the flat were removed with a fringe map, which was the median of the sky subtracted data that was then smoothed with a 5×5 pixel box. The spectra were then combined, extracted, and calibrated in wavelength and flux.

The reduced spectrum of 2001gq is shown in Figure A3.

2.3. Spectral Fitting and Supernova Typing

Light from the host and the SN is often strongly blended in the spectra of high redshift SN. To separate the two, we followed the spectral fitting technique described in Howell et al. (2005).

To classify the SNe, we used the classification scheme described in Lidman et al. (2005) and added to it the confidence index (CI) described in Howell et al. (2005). In the Lidman et al. (2005) scheme, an object is classified as an SN Ia if the Si II features at 4000 Å and/or 6150 Å or the S II W feature can be clearly identified in the spectrum or if the spectrum is best fit with the spectra of nearby SN Ia and other types do not provide a good fit. We qualify the classification with the keys "Si II" or "SF" in Column 3 of Table 3 depending on whether the classification was done by identifying features or by using the fit. In the scheme described in Howell et al. (2005), these SNe would have a CI of 5 and 4, respectively.

Less secure candidates are classified as Ia*. The asterisk indicates some degree of uncertainty. Usually, this means that we can find an acceptable match with nearby SNe Ia; however, other types, such as SNe Ibc, also result in acceptable matches. These SNe have a CI of 3.

Redshifts based on the host have an accuracy that is better than 0.001, and are, therefore, quoted to three decimal places. Redshifts based on the fit are less accurate. For completeness, the redshifts and classifications reported in Lidman et al. (2005) and Morokuma et al. (2010) are also included.

The agreement between the phase, $t_{\rm Spec}$, of the best-fit template and the corresponding phase, $t_{\rm LC}$, obtained from the light-curve fit is also shown in Table 3. The weighted average difference for all six spectra is $\Delta t = -0.4$ days with a dispersion of 2.0 days. The dispersion is similar in magnitude to that found in other surveys (Hook et al. 2005; Foley et al. 2008).

3. PHOTOMETRIC OBSERVATIONS

A total of nine different instruments, listed in Table 4, were used for the photometric follow-up of the SNe described in this work.

All observations are listed in Table B1. Here, the modified Julian Date (MJD) is the weighted average of all images taken during a given night except for the NIR data where data taken over several nights were combined. We do not report the MJD for combined reference images that were taken over several months.

3.1. Ground-based Optical Observations and Reductions

We obtained ground-based optical follow-up data of the SNe through different combinations of passbands, shown in Figure 2, similar to Bessel *R* and *I* (Bessell 1990), and SDSS *i* (Fukugita et al. 1996). Here we used FORS1 (Appenzeller et al. 1998) at VLT and SuSI2 (D'Odorico et al. 1998) at NTT in addition to the search instruments. The SuSI2, MOSAIC II, CFH12k, and SuprimeCam data were obtained in the visitor mode, while the FORS1 observations were carried out in the service mode.

All optical ground data were reduced (Raux 2003) in a standard manner including bias subtraction, flat fielding, and fringe map subtraction using the IRAF[29] software.

[29] IRAF is distributed by the National Optical Astronomy Observatory, which is operated by the Association of Universities for Research in Astronomy, Inc., under the cooperative agreement with the National Science Foundation.

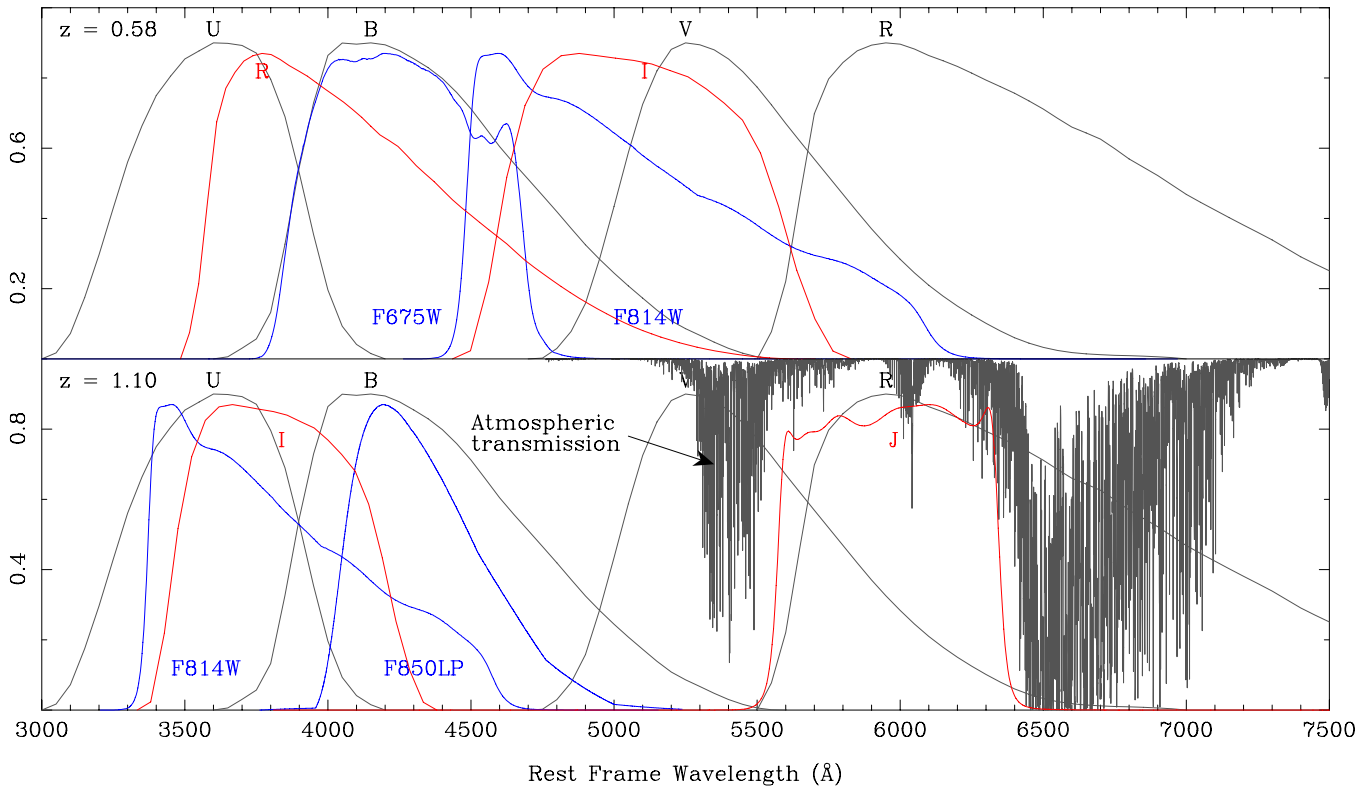

Figure 2. Illustration of filters (colored) used in the SN campaign together with the rest frame Bessel filters (gray). The red (ground-based) and blue (*HST*) filters were used for the observations of the three SNe below (upper panel) and above (lower panel) $z = 0.7$, respectively. The filters have been blueshifted to the mean of the two sub samples. Note that the Bessel filters shown here differ slightly from the corresponding filters used at the different telescopes. Not shown in the figure is the SuprimeCam *i* filter, which is close to the *I* filter and was only used for 2001cw. We show the *J*-band filter curve for NIRI which is very similar to the ISAAC *Js* filter. The atmospheric transmission for 2 mm of precipitable water vapor, typical for Paranal and Mauna Kea, is also plotted between 10000 and 16000 Å in the observer frame. The transmission curve was provided by A. Smette (2009, private communication).

(A color version of this figure is available in the online journal.)

3.2. Ground-based IR Observations and Reduction

The two most distant SNe in the sample, 2001hb and 2001gn, were also observed from the ground in the near-IR. Both NIRI (Hodapp et al. 2003) and ISAAC (Moorwood et al. 1999) were used to observe 2001hb, while 2001gn was observed with ISAAC only.

The ISAAC observations were done with the *Js* filter and the NIRI observations were carried out with the *J* filter. The transmission curves of the filters are similar to each other, and the transmission curve of the latter is shown in Figure 2. The red edges of the filters are defined by the filters and not by the broad telluric absorption band that lies between the *J* and *H* windows, and the central wavelength is slightly redder than the central wavelength of the *J* filter of Persson et al. (1998). Compared to traditional *J*-band filters, photometry with the ISAAC *Js* and NIRI *J*-band filters is less affected by water vapor and is therefore more stable.

The ISAAC observations were done in the service mode and the data were taken on 14 separate nights, starting on 2001 May 7 and ending on 2003 May 30. Individual exposures lasted 30–40 s, and three to four of these were averaged to form a single image. Between images, the telescope was offset by 10″–30″ in a semi-random manner, and typically 20–25 images were taken in this way in a single observing block. The observing block was repeated several times until sufficient depth was reached.

The data, including the calibrations, were first processed to remove two electronic artifacts. In about 10% of the data, a difference in the relative level of odd and even columns can be seen. The relative difference is a function of the average count level and it evolves with time, so it cannot be removed with flat fields. In those cases where the effect is present, the data are processed with the `eclipse`[30] odd–even routine. The second artifact, an electronic ghost, which is most easily seen when there are bright stars in the field of view, is removed with the `eclipse` ghost routine.

The NIRI observations were done in the queue mode and the data were taken on 4 separate nights, starting on 2001 May 25 and ending on 2002 August 5. Individual exposures lasted 60 s. Between images, the telescope was offset by 10″–30″ in a semi-random manner, and typically 60 images were taken in this way in a single observing sequence. The sequence was repeated several times until sufficient depth was reached.

Both the ISAAC and NIRI data were then reduced in a standard way with the IRAF XDIMSUM package and our own IRAF scripts. From each image, the zero-level offset was removed, a flat field correction was applied, and an estimate of the sky from other images in the sequence was subtracted. Images were then combined with individual weights that depend on the median sky background and the image quality.

3.3. HST Observations and Reduction

Observing SN Ia at high-*z* from space has an enormous advantage for accurately following their light curves. The absence of the atmosphere and the high spatial resolution allows

[30] http://www.eso.org/sci/data-processing/software/eclipse

high signal-to-noise measurements. The high spatial resolution also helps minimize host contamination through focusing the light over a smaller area. Space also permits observations at longer wavelengths where the limited atmospheric transmission and the high background degrade ground-based data.

High-quality follow-up data were obtained for all six SNe using the WFPC2 on the *HST* during Cycle 9. All but two (2001cw and 2001gq) of the objects also have SN-free reference images taken during Cycle 10, with the ACS. WFPC2 consists of four 800 × 800 pixel chips of which one, the Planetary Camera (PC), has twice the resolution of the others. The SNe were always targeted with the lower left corner of the PC in order to place them closer to the readout amplifier so that the effects of charge-transfer inefficiency would be reduced. Images of the same target were obtained with roughly the same rotation for all epochs.

Each SN was followed in two bands. All SNe were observed in the *F814W* filter. Additionally, the *F675W* filter was used for the three SNe at $z < 0.7$ and the *F850LP* filter was used for the high redshift targets. These filters were chosen to match the filters used on the ground and correspond approximately to rest-frame *UBV* bands as illustrated in Figure 2.

The data were reduced with software provided by the Space Telescope Science Institute (STScI). WFPC2 images were processed through the STScI pipeline and then combined for each epoch to reject cosmic rays using the `crrej` task which is part of STSDAS[31] IRAF package.

The ACS images were processed using the multi-drizzle (Fruchter & Hook 2002) software, which also corrects for the severe geometric distortion of the instrument. For this we used the updated distortion coefficients from the ACS Data Handbook in 2006 November, and drizzled the images to the resolution of the WFPC2 images 0.″046. Note that the WFPC2 images were *not* corrected for geometric distortion at this stage.

4. PHOTOMETRY OF THE GROUND-BASED DATA

The photometry technique applied to the optical ground-based data is the same as the one applied in Amanullah et al. (2008), except for the SuprimeCam *i*-band data. This is also very similar to the method (Fabbro 2001) used in Astier et al. (2006) and is briefly summarized here.

1. Each exposure of a given SN in a given passband was aligned to the best seeing *photometric reference* image.
2. In order to properly compare images of different image quality we fitted convolution kernels, K_i, modeled by a linear decomposition of Gaussian and polynomial basis functions (Alard & Lupton 1998; Alard 2000), between the photometric reference and each of the remaining images, i, for the given passband. The kernels were fitted by using image patches centered on fiducial objects across the field.
3. The background sky level for each image, i, is not expected to have any spatial variation for a small patch, $I_i(x, y)$, centered on the SN with a radius of the worst seeing FWHM. We assume that the patch can be modeled by a point-spread function (PSF) at the location of the SN, a model of the host galaxy and a constant offset for the sky,

$$I_i(x, y) = f_i \cdot [K_i \otimes \mathrm{PSF}](x - x_0, y - y_0) + [K_i \otimes G](x, y) + S_i \, .$$

For a time series of such patches we simultaneously fit the SN position, (x_0, y_0), and brightnesses, f_i, the host model, $G(x, y)$, and background sky levels, S_i. We use a non-analytic host model with one parameter per pixel. This means that the model will be degenerated with the SN and the sky background. We break these degeneracies by fixing the SN flux to zero for all reference images and fix the sky level to zero in one of the images. Figure 3 shows an example of image patches, galaxy model residuals, and resulting residuals when the full model has been subtracted, for increasing epochs.

The SN light curves were obtained in this manner for one filter and instrument at a time where SN-free reference images were available. In the cases where SN-free references did not exist for a given telescope, reference images obtained with other telescopes were used instead.

For the IR image of 2001hb, we performed aperture photometry directly on the images, assuming the SN to be hostless for the purpose of *J*-band photometry, since no host could be detected at the limit of the ACS references (see below). For the IR image of 2001gn, we carried out steps (1)–(2) above, and then subtracted the reference image (Figure 4) and did aperture photometry on the resulting image. In both cases, the SN positions from the *HST* images were used for centroiding the aperture and the diameter was chosen to maximize the signal-to-noise ratio. The fluxes are corrected to larger apertures by analyzing bright stars in the same image.

The *i*-band data for 2001cw were analyzed together with a larger sample of SNe discovered at Subaru. The details of this analysis are given in N. Yasuda et al. (2010, in preparation).

4.1. Calibration of the Ground-based Data

Nightly observations of standard stars were not available for all optical instruments and filters. Instead the recipe from Amanullah et al. (2008), using SDSS (Adelman-McCarthy et al. 2007) measurements of the field stars was applied. However, the SDSS filter system (Fukugita et al. 1996) differs significantly from the filters used in this search except for the SuprimeCam *i* band. To overcome this difference, we fitted relations between the SDSS filter system and the Landolt system (Landolt 1992) in a similar manner to Lupton (2005), using stars with SDSS and Stetson photometry (Stetson 2000). Stetson has been publishing photometry of a growing list of faint stars that is tied to the Landolt system within 0.01 mag (Stetson 2000). The most up-to-date version can be obtained from the Canadian Astronomy Data Center.[32] In contrast to Lupton (2005), we applied magnitude, uncertainty, and color cuts ($15 < r_{\mathrm{SDSS}} < 18.5$, $\sigma_m < 0.03$ mag in r_{SDSS} and i_{SDSS} and $-0.5 < r_{\mathrm{SDSS}} - i_{\mathrm{SDSS}} < 1.0$) for the stars that went into the fit. We also applied a 5σ outlier cut after our initial fit (and lost about ∼6% of the sample). After refitting, the following relations were derived for the Landolt *R* and *I* filters

$$R - r_{\mathrm{SDSS}} = -0.13 - 0.32 \cdot (r_{\mathrm{SDSS}} - i_{\mathrm{SDSS}})$$
$$I - i_{\mathrm{SDSS}} = -0.38 - 0.26 \cdot (r_{\mathrm{SDSS}} - i_{\mathrm{SDSS}}),$$

which are also shown in Figure 5. The results for $R - r_{\mathrm{SDSS}}$ are close to the ones derived by Lupton (2005) as well as to Tonry et al. (2003) who performed a similar operation. Neither Tonry et al. (2003) nor Lupton (2005) present fits for $I - i_{\mathrm{SDSS}}$ versus $r_{\mathrm{SDSS}} - i_{\mathrm{SDSS}}$.

[31] The Space Telescope Science Data Analysis System (STSDAS) is a software package for reducing and analyzing astronomical data. It provides general-purpose tools for astronomical data analysis as well as routines specifically designed for *HST* data.

[32] http://www.cadc.hia.nrc.gc.ca/community/STETSON/archive/

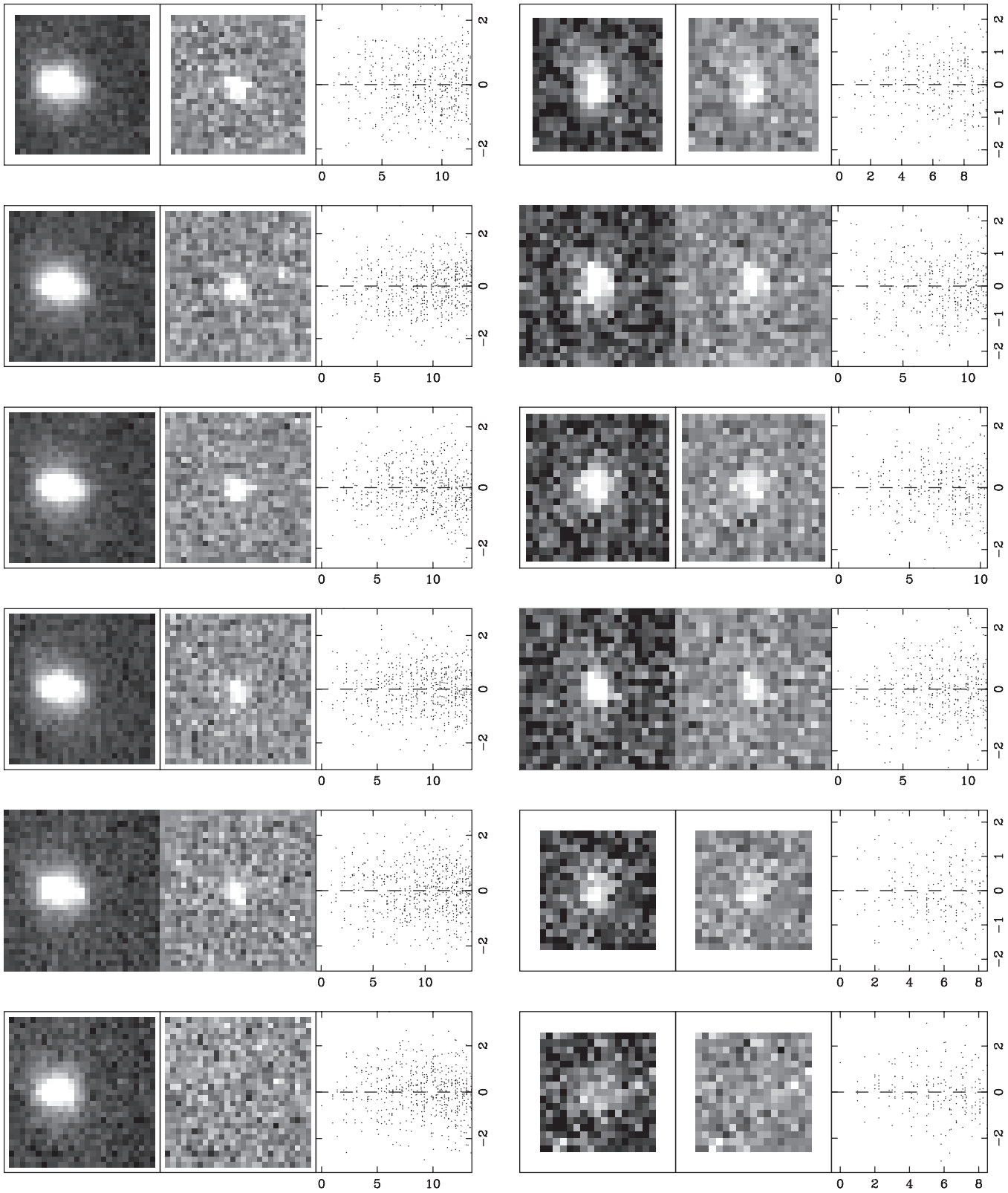

Figure 3. Ground-based *I*-band images (patches) of 2001gq (three left columns; width 6.″0) and 2001go (three right columns; width 4.″7). Each triplet represents from left to right the fully reduced data, the galaxy model subtracted data, and a profile plot where the full galaxy + PSF model has been subtracted from the data. The profile plot shows the deviation from zero in standard deviations of the noise vs. the distance from the SN position in pixels. Epoch increases from top to bottom. The images in the last row are the reference image, obtained approximately one year after discovery. The different image sizes (patches) reflect differences in image quality. A small image represents good seeing conditions.

By forcing $\chi^2/\mathrm{dof} = 1$, we determined that there is a scatter of 0.03 mag coming from intrinsic spectral distributions. This is a systematic uncertainty for individual stars, but will average out when a big sample is used, assuming that the color

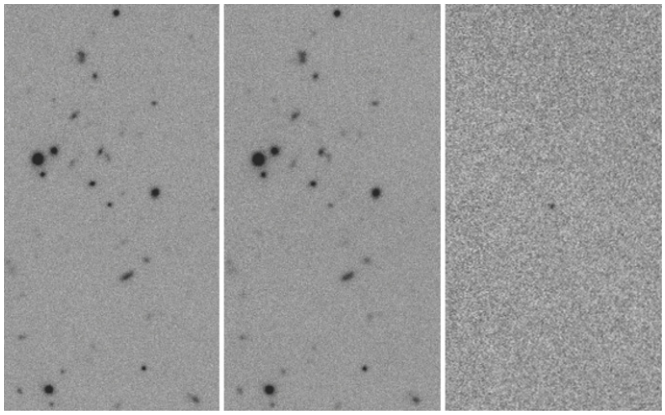

Figure 4. VLT/ISAAC *J*-band observations of the distant SN Ia, 2001gn (north is up and east is to the left). On the left, we show a 27″ wide and 51″ high image with the SN ; in the middle we show the reference image, which was taken two years later. The images on the right are the subtraction between the two and show the SN with a signal-to-noise ratio of 10. Each image is the result of 10 hr of integration in good conditions. The image quality in the left-hand image is FWHM = 0.″39.

distribution of the sample is similar to the stars used to derive the relations.

The transformations were applied to the SDSS stellar photometry of our SN field, and these were then used as tertiary standard stars in order to tie the SN photometry to the Landolt system. The flux of the stars was determined on the photometric reference for each light curve build using the same method as for the SN and with the same PSF model that was used for fitting the SN fluxes. A zero-point relation of the form

$$m + 2.5 \log_{10} f = \mathrm{ZP} + c_X \cdot (R - I) \quad (1)$$

could then be fitted between the measured stellar fluxes, f, and their Landolt magnitudes, m. Here ZP is the zero point and c_X is the color term for the filter. We applied the same color cuts ($-0.5 < r_{\mathrm{SDSS}} - i_{\mathrm{SDSS}} < 1.0$) to the stars that went into the fit.

Unfortunately we did not have enough stars over a wide enough color range to accurately fit the color term. Instead, we used values from the literature or from the observatories, which are summarized in Table 5. The zero points could then be derived from Equation (1). The values obtained this way are the sums of three components; the instrumental zero point, the aperture correction to the PSF normalization radius, and the atmospheric extinction for the given airmass, and are shown along with the SN fluxes in Table B1.

We also calculated color terms synthetically by using Landolt standard stars that have extensive spectrophotometry from Stritzinger et al. (2005). The synthetic Vega magnitudes of the stars were calculated by multiplying the spectra and the Vega spectrum (Bohlin 2007) with the filter and instrument throughputs provided by the different observatories. The color terms were then fitted by assuming a linear relation for the deviation between the synthetic and the Landolt magnitudes as a function of the Landolt color. The resulting fitted synthetic terms are also presented in Table 5.

The difference is $\lesssim$0.03 mag for all but the CFH12k *I* band, where there is a significant discrepancy. A mismatch between the effective filter transmission curves we use and the true photometric system is most likely the origin of this.

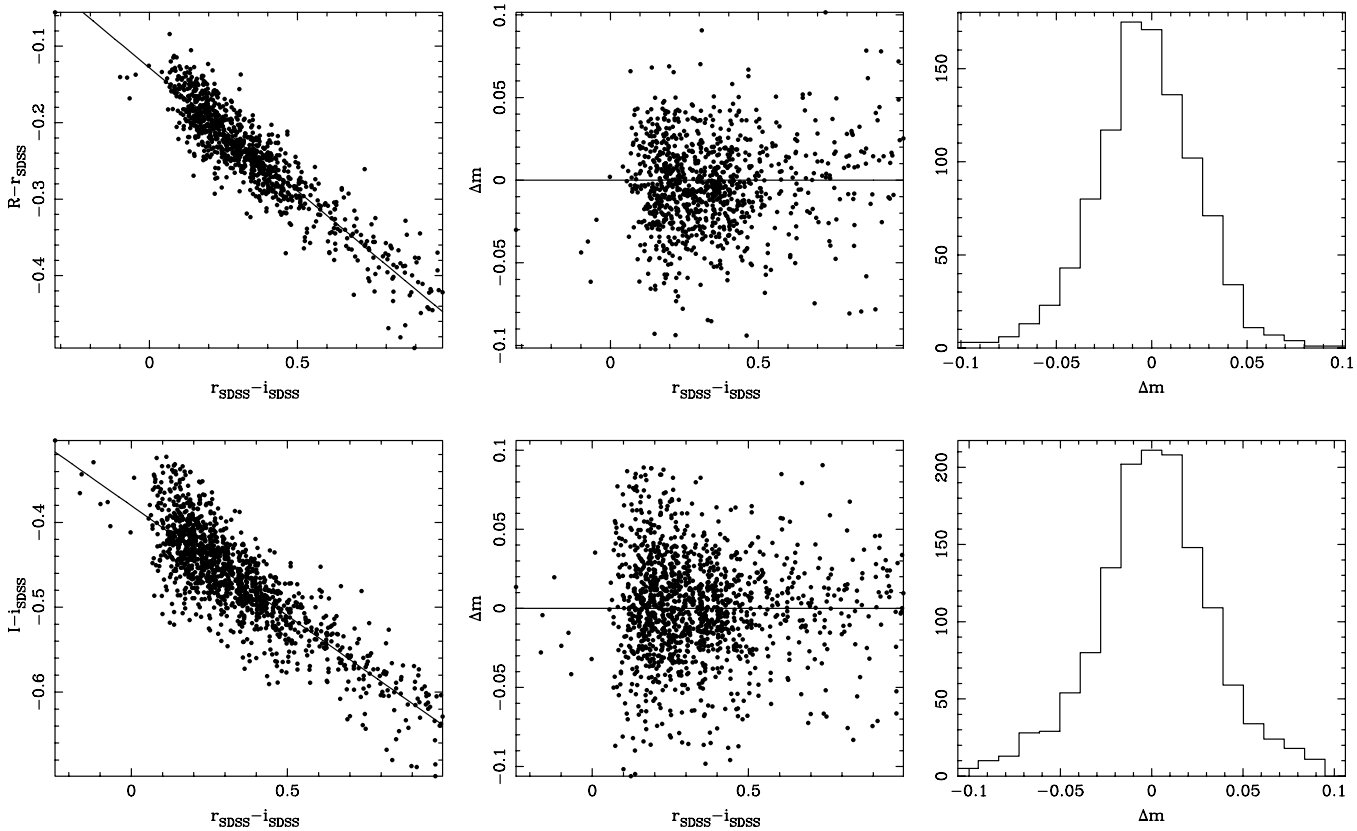

Figure 5. Stars observed both by Stetson (2000) and SDSS for which $-0.5 < r_{\mathrm{SDSS}} - i_{\mathrm{SDSS}} < 1.0$ together with fitted linear relations between the SDSS r_{SDSS}, i_{SDSS} and the Landolt R, I magnitudes. The left column shows the relation as a function of color, while the middle column shows the residuals once the fitted relation has been subtracted, and a histogram of the residuals are presented in the right column.

Table 5
Measured and Synthetic Color Terms for the Three Instruments that were Used as Photometric References

Instr./Tel.	Measured		Synthetic	
	c_R	c_I	c_R	c_I
CFH12k/CFHT	0.031[a]	0.107[a]	0.066	−0.023
MOSAIC II/CTIO	...	0.030[b]	...	0.007
FORS1/VLT	0.034[c]	−0.050[c]	0.040	−0.076

Notes.
[a] http://www.cfht.hawaii.edu/Instruments/Elixir/filters.html
[b] Miknaitis et al. (2007).
[c] http://www.eso.org/observing/dfo/quality/FORS1/qc/photcoeff/photcoeffs_fors1.html

We have investigated if the deviation could be explained by the differences in quantum efficiencies between the different chips of the detector which are presented on the CFH12k Web page. However, these differences propagated to the color term result in relatively low scatter and deviate significantly from the measured value.

For the purpose of fitting the zero points, we can use the measured color terms, but for light-curve fitting erroneous filter transmissions could introduce systematic effects. In order to study the potential impact on the light-curve fits we modified the filters to match the measured color terms. The modifications were implemented by either shifting or clipping the filters until the synthetic color terms matched all measured values for a given filter (e.g., R or I versus $R-I$, $V-I$, and $B-I$ for the ELIXIR measurements for the I band). The light curves were then refitted using the modified filter transmissions and the resulting values were compared. Since the light curves are tightly constrained by the high-precision *HST* data, the modified filter only leads to negligible differences (less than 30% of the statistical uncertainty) in the fitted parameters.

The J-band data, on the other hand, were calibrated using G-type standard stars from the Persson LCO standard star catalog (Persson et al. 1998). Since the ISAAC and NIRI J-band filters are slightly redder and narrower than the Persson J-band filter, we subtracted 0.012 mag from the ISAAC and NIRI zero points to place the ISAAC and NIRI IR photometry onto the natural system. Since the data were taken over many nights, the photometry was carefully cross-checked. Differences in the absolute photometry usually amount to less than 0.02 mag, which we conservatively adopt as our zero-point uncertainty.

5. PHOTOMETRY OF THE *HST* DATA

A modified version of the photometric technique from Knop et al. (2003) was used for the *HST* data presented here. This is similar to the method used for the ground-based optical data above, but instead of aligning and resampling all images to a common frame, the host+SN model is resampled to each individual image. A procedure like this is preferred when the PSF FWHM is of the same order as the pixel scale, and it also preserves the image noise properties.

Linear geometric transformations were first fitted from each image, k, in a given filter to the deepest image of the field using field objects. Due to the similar orientation of the WFPC2 images, linear transformations were sufficient for these, and the geometric distortion of WFPC2 could be ignored. This was however not the case for the transformations between the ACS and WFPC2 images and the distortion was then hardcoded into the fitting procedure. Due to the sparse number of objects in the tiny PC field the accuracy of all transformations was only good to $\lesssim 1$ pixel ($\sim$0.5 FWHM). Unfortunately, using objects from the remaining three chips for the alignment did not lead to improved accuracy, which is probably due to small movements of the chips between exposures (Anderson & King 2003). This alignment precision was not enough for PSF photometry, and we therefore allowed the SN position, (x_{k0}, y_{k0}) to float for the individual images which increased the alignment precision by a factor of 10. Allowing this extra degree of freedom could bias the results toward higher fluxes since the fit will favor positive noise fluctuations. However, as in Knop et al. (2003), this was shown to be of minor importance by studying the covariance between the fitted flux and SN position.

The full model used to describe each image patch can be expressed as

$$I_k(x_k, y_k) = f_k \cdot \mathrm{PSF}_k(x_k - x_{k0}, y_k - y_{k0}) + G(x_k, y_k, a_j) + S_k \,. \quad (2)$$

Here I_k is the value in pixel (x_k, y_k) on image k, f_k is the SN flux, PSF_k is the point spread function, G is the host galaxy model that is parameterized by a_j, and S_k is the local sky background. The fits were carried out using a χ^2 minimization approach using MINUIT (James & Roos 1975).

Four SNe in the sample had ACS reference images, and for these cases we used field objects to fit non-analytic convolution kernels, K, between the PC chip and the drizzled ACS image. These accounted for the difference in quantum efficiency and PSF shape between the two instruments. When kernels were used, the uncertainties of individual pixels were propagated and the correlation between pixels produced by the convolution were taken into account. Also, in this case Equation (2) above was modified so with both the PC images and the PC PSF being convolved with the fitted kernel.

The PSF, PSF_k, of the WFPC2 PC chip was simulated for each filter and pixel position using the Tiny Tim software (Krist 2001) and normalized to the WFPC2 calibration radius 0.″5. We also did an extensive test where we iteratively updated the simulated PSF based on the knowledge of the SN epoch, and therefore the approximate spectral energy distribution (SED), but this did not have any significant effect on the fitted fluxes. The Tiny Tim PSF was generated to be subsampled by a factor of 10. For each iteration in the fitting procedure, any shift of the PSF position was first applied in the subsampled space. The PSF was then rebinned to normal sampling and convolved with a *charge diffusion kernel* (Krist 2001) before it was added to the patch model.

For three of the SNe, 2001cw, 2001gq, and 2001hb we used an analytical model for the host galaxy. Both 2001cw and 2001gq are offset from the core of their respective host galaxies and we therefore chose not to obtain SN-free reference images for these. Instead the hosts could be modeled by a second-order polynomial and constrained by the galaxy light in the vicinity of the SNe. For 2001hb, we did obtain a deep ACS reference image but no host could be detected. For this SN we used a simple plane to model the host which was further constrained by fixing the SN flux to zero for the ACS reference. One caveat with analytical host modeling in general is that the patch size must be chosen with care. The model will only work if there is no dramatic change in the background across the patch, which is an assumption that is likely to fail if the patch is too large and includes the host galaxy core. On the other hand, the patch cannot be too small either in order to successfully break the degeneracy between the SN and the background.

To make sure that the choice of the host model does not bias the fitted SN fluxes we required, in addition to clean residuals once the SN + host was subtracted from the data, that the fitted SN fluxes were insensitive to variations in the patch size of a few pixels. Further, for 2001gq, we tested the host model by putting fake SNe at different positions around the core of the host. The distances to the core and the fluxes of the fakes were always chosen to match the corresponding values for the real SN, and the retrieved photometry was always within the expected statistical uncertainty.

The recipe described above could not be used for the remaining three SNe in the sample, since they were located too close to the cores of their host galaxies. Additionally, the hosts have small angular sizes and the light gradients in the vicinity of the SNe were steep enough to lead to biased photometry due to the coarse geometric alignment. To overcome this we changed the photometric procedure slightly. Instead of fitting the SN position on each image, we chose to fit it only on the geometric reference image, and then introduce a free shift for the whole model. That is, in this case we used the galaxy model + SN for the patch alignment. However, this procedure did force us to apply some constraints on the galaxy modeling. Using a non-analytic pixel model, the approach used for the ground-based optical data was not feasible. It slowed down the fits considerably and rarely converged. Instead we chose to use the ACS images of the host galaxies directly. The ACS references were much deeper then the WFPC2 data and choosing this procedure did not increase the uncertainty of the fitted fluxes.

A general problem with doing photometry on *HST* images is that CCD photometry of faint objects over a low background suffers from an imperfect charge transfer, which will lead to an underestimate of the flux. We used the charge transfer efficiency (CTE) recipe for point sources from Dolphin (2009). The correction for our data is usually around 5%–8% but it can be as large as ∼17%. The uncertainties of the corrections were propagated to the flux uncertainties. The corrected SN fluxes are given in Table B1 together with the instrumental zero-points, which were also obtained from Andrew Dolphin's Web page.

6. LIGHT-CURVE FITTING

SN Ia that has bluer colors or broader light curves tends to be intrinsically brighter (Phillips 1993; Tripp 1998). Several methods of combining this information into an accurate measure of the relative distance have been used (Riess et al. 1996; Goldhaber et al. 2001; Wang et al. 2003; Guy et al. 2005, 2007; Jha et al. 2007; Conley et al. 2008).

K08 consistently fitted all light curves using the SALT (Guy et al. 2005) fitter, which is built on the SN Ia SED from Nugent et al. (2002). In this paper, we use SALT2 (Guy et al. 2007), which is based on more data.

Conley et al. (2008) compared the performances of different light-curve fitters while also introducing their own empirical fitter, SiFTO, and concluded that SALT2 along with SiFTO perform better than both SALT (which is conceptually different from its successor SALT2) and MLCS2k2 (Jha et al. 2007) when judged by the scatter around the best-fit luminosity–distance relationship. Furthermore, SALT2 and SiFTO produce consistent cosmological results when both are trained on the same data. Recently KS09 made a thorough comparison between SALT2 and their modified version of MLCS2k2 for a compilation of public data sets, including the one from the SDSS SN survey. The two light-curve fitters result in an estimate of w (for a flat wCDM cosmology) that differs by 0.2. The difference exceeds their statistical and systematic (from other sources) error budgets. They determine that this deviation originates almost exclusively from the difference between the two fitters in the rest-frame U-band region, and the color prior used in MLCS2k2. They also noted that MLCS2k2 is less accurate at predicting the rest-frame U band using data from filters at longer wavelengths.

This difference in U-band performance is not surprising: observations carried out in the observer-frame U band are in general associated with a high level of uncertainty due to atmospheric variations. While the training of MLCS2k2 is exclusively based on observations of nearby SNe, the SiFTO and SALT2 trainings address this difficulty by also including high redshift data where the rest-frame U band is observed at redder wavelengths. This approach also allows these fitters to extend blueward of the rest-frame U band.

In addition, for this paper, we have conducted our own test validating the performance of SALT2 by carrying out the Monte Carlo simulation described in Section 7.3.6, where we compare the fitted SALT2 parameters to the corresponding real values for mock samples with poor cadence and low signal to noise drawn from individual well-measured nearby SNe.

Given these tests that have been carried out on SALT2, and its high redshift source for rest-frame U band, we have chosen to use SALT2 in this paper.

6.1. SALT2

The SALT2 SED model has been derived through a pseudo-principal component analysis based on both photometric and spectroscopic data. Most of these data come from nearby SN Ia data, but SNLS SNe are also included. To summarize, the SALT2 SED, $F(\mathrm{SN}, p, \lambda)$, is a function of both wavelength, λ, and time since B-band maximum, p. It consists of three components; a model of the time-dependent average SN Ia SED, $M_0(p, \lambda)$, a model of the variation from the average, $M_1(p, \lambda)$, and a wavelength-dependent function that warps the model, $\mathrm{CL}(\lambda)$. The three components have been determined from the training process (Guy et al. 2007) and are combined as

$$F(\mathrm{SN}, p, \lambda) = x_0 \times [M_0(p, \lambda) + x_1 \times M_1(p, \lambda)] \times \exp[c \times \mathrm{CL}(\lambda)],$$

where x_0, x_1, and c are free parameters that are fit for each individual SN.

Here, x_0, describes the overall SED normalization, x_1, the deviation from the average decline rate ($x_1 = 0$) of an SN Ia, and c, the deviation from the mean SN Ia $B-V$ color at the time of B-band maximum. These parameters are determined for each observed SN by fitting the model to the available data. The fit is carried out in the observer frame by redshifting the model, correcting for Milky Way extinction (using the CCM-law from Cardelli et al. 1989 with $R_V = 3.1$), and multiplying by the effective filter transmission functions provided by the different observatories. All synthetic photometry is carried out in the Vega system using the spectrum from Bohlin (2007). Following Astier et al. (2006) we adopt the magnitudes $(U, B, V, R_C, I_C) = (0.020, 0.030, 0.030, 0.030, 0.024)$ mag (Fukugita et al. 1996) for Vega. For the near-infrared we adopt the values $J = 0$ and $H = 0$.

In the fit to our data, we take into account the correlations introduced between different light-curve points from using the same host galaxy model. We also chose to run SALT2 in the mode where the diagonal of the covariance matrix is updated iteratively in order to take model and K-correction uncertainties

Table 6
Light-curve Fit Results Using SALT2

SN	$\mathrm{MJD_{max}}$	m_B^{corr}	m_B^{max}	c	x_1	s
2001cw	52066.60 ± 0.86	24.88 ± 0.42	24.71 ± 0.13	−0.10 ± 0.36	0.140 ± 0.844	0.993 ± 0.077
2001gn	52030.33 ± 0.16	25.16 ± 0.23	25.37 ± 0.05	0.07 ± 0.05	0.648 ± 0.649	1.040 ± 0.061
2001go	52010.99 ± 0.35	23.13 ± 0.11	23.08 ± 0.07	−0.11 ± 0.07	−1.149 ± 0.259	0.881 ± 0.022
2001gq	52028.81 ± 0.42	23.62 ± 0.19	23.79 ± 0.03	0.06 ± 0.04	0.459 ± 0.287	1.022 ± 0.027
2001gy	52031.66 ± 0.25	22.97 ± 0.07	23.05 ± 0.03	−0.03 ± 0.03	−0.312 ± 0.265	0.952 ± 0.024
2001hb	52038.02 ± 0.97	24.84 ± 0.13	24.79 ± 0.03	0.00 ± 0.04	1.292 ± 0.410	1.101 ± 0.039

Notes. The SALT2 parameters are $\mathrm{MJD_{max}}$, m_B, x_0, x_1, and c. Here, the light-curve shape, x_1, and color, c, corrected peak B-band magnitude are obtained from Equation (3) as $m_B^{\mathrm{corr}} = m_B^{\mathrm{max}} + \alpha \cdot x_1 - \beta \cdot c$, where the values $\alpha = 0.12$ and $\beta = 2.51$ have been used. For comparison we also present the SALT stretch, s, which has been derived from x_1 using the relation provided in Guy et al. (2007).

into account. See Guy et al. (2007) for details on this. The Milky Way reddening for our SNe from the Schlegel et al. (1998) dust maps is given in Table 2. The results of the fits are shown in Table 6 and plotted in Figure 6 together with the data.

The three parameters $m_B^{\mathrm{max}} = -2.5 \log_{10} [\int_B F(\mathrm{SN}, 0, \lambda)\, \lambda\, d\lambda]$, x_1 and c, can for each SN be combined to form the distance modulus (Guy et al. 2007),

$$\mu_B = m_B^{\mathrm{corr}} - M_B = m_B^{\mathrm{max}} + \alpha \cdot x_1 - \beta \cdot c - M_B, \qquad (3)$$

where M_B is the absolute B-band magnitude. The resulting color and light-curve shape corrected peak B-band magnitudes, m_B^{corr}, are presented in the third column of Table 6. The parameters α, β, and M_B are nuisance parameters which are fitted simultaneously with the cosmological parameters.

7. THE UNION2 COMPILATION

K08 presented an analysis framework for combining different SN Ia data sets in a consistent manner. Since then two other groups (H09 and KS09) have made similar compilations, using different fitters. In this work, we carry out an improved analysis, using and refining the approach of K08. We extend the sample with the six SNe presented here, the SNe from Amanullah et al. (2008), the low-z and intermediate-z data from Hicken et al. (2009b) and Holtzman et al. (2008), respectively.[33]

First, all light curves are fitted using a single light-curve fitter (the SALT2 method) in order to eliminate differences that arise from using different fitters. For all SNe going into the analysis we require

1. data from at least two bands with rest-frame central wavelengths between 2900 Å and 7000 Å, the default wavelength range of SALT2;
2. that there is at least one point between −15 days and 6 rest-frame days relative to the B-band maximum;
3. that there are in total at least five valid data points available;
4. that the fitted x_1 values, including the fitted uncertainties, lie between $-5 < x_1 < 5$. This is a more conservative cut than that used in K08 and results in several poorly measured SNe being excluded. Part of the discrepancy observed by KS09 when using different light-curve models could be traced to poorly measured SNe; and
5. that the CMB-centric redshift is greater than $z > 0.015$.

We also exclude one SN from the Union compilation that is 1991bg-like, which neither the SALT nor the SALT2 models are trained to handle. Note that another 1991bg-like SN from the Union compilation was removed by the outlier rejection. All SNe Ia considered in this compilation are listed in Table B2. For each SN, the redshift and fitted light-curve parameters are presented as well as the failed cuts, if any.

It should be pointed out that the choice of the light-curve model also has an impact on the sample size. Using SALT2 will allow more SNe to pass the cuts above, since the SALT2 model covers a broader wavelength range than SALT. This is particularly important for high-z data that heavily rely on rest-frame *UV* data. For example, two net SNe would have been cut from the Riess et al. (2007) sample with the SALT model.

7.1. Revised HST Zero Points and Filter Curves

Since Riess et al. (2007), the reported zero points of both NICMOS and ACS were revised. For the *F110W* and *F160W* filters of NICMOS, the revision is substantial. Using the latest calibration (Thatte et al. 2009 and references within), the revised zero points are, for both filters, approximately 5% fainter than those reported in Riess et al. (2007) and subsequently used by K08.

For SNe Ia at $z > 1.1$, observations with NICMOS cover the rest-frame optical, so the fitted peak B-band magnitudes and colors and the corrected B-band magnitudes of these SNe Ia depend directly on the accuracy of the NICMOS photometry. With the new zero points, SNe Ia at $z > 1.1$ are measured to be fainter and bluer. Our current analysis also corrects an error in the NICMOS filter curves that were used in K08, which also acts in the same direction.

In the Introduction, we had noted that almost all SNe at $z > 1.1$ were redder than the average SN color over the redshift interval 0.3–1.1. This is surprising as redder SNe are also fainter and should therefore be the harder to detect in magnitude limited surveys. K08 noted that these SNe, after light-curve shape and color corrections, are also on average ∼0.1 mag brighter than the line tracing the best-fit ΛCDM cosmology. They also noted that this was the reason for the relatively high value for the binned value of w in the [0.5, 1] redshift bin.

After taking the NICMOS zero-point and filter updates just discussed into account, we repeated the original K08 analysis. This made the NICMOS observed SNe up to ∼0.1 mag fainter, and there no longer is a significant offset from the best-fit cosmology. Nor are these SNe unusually red when compared to SNe over the redshift interval 0.3–1.1. For SALT2 the SNe at $z > 1.1$ have an average color of $c = 0.06 \pm 0.03$, compared to $c = 0.02 \pm 0.01$ for $0.3 < z < 1.1$, and no significant offset in the Hubble diagram.

There could however still be unresolved NICMOS issues. For example, the NICMOS SN photometry depends on extrapolat-

[33] The SALT2 fit results for these samples are presented along with the entire Union2 compilation fits at http://supernova.lbl.gov/Union/.

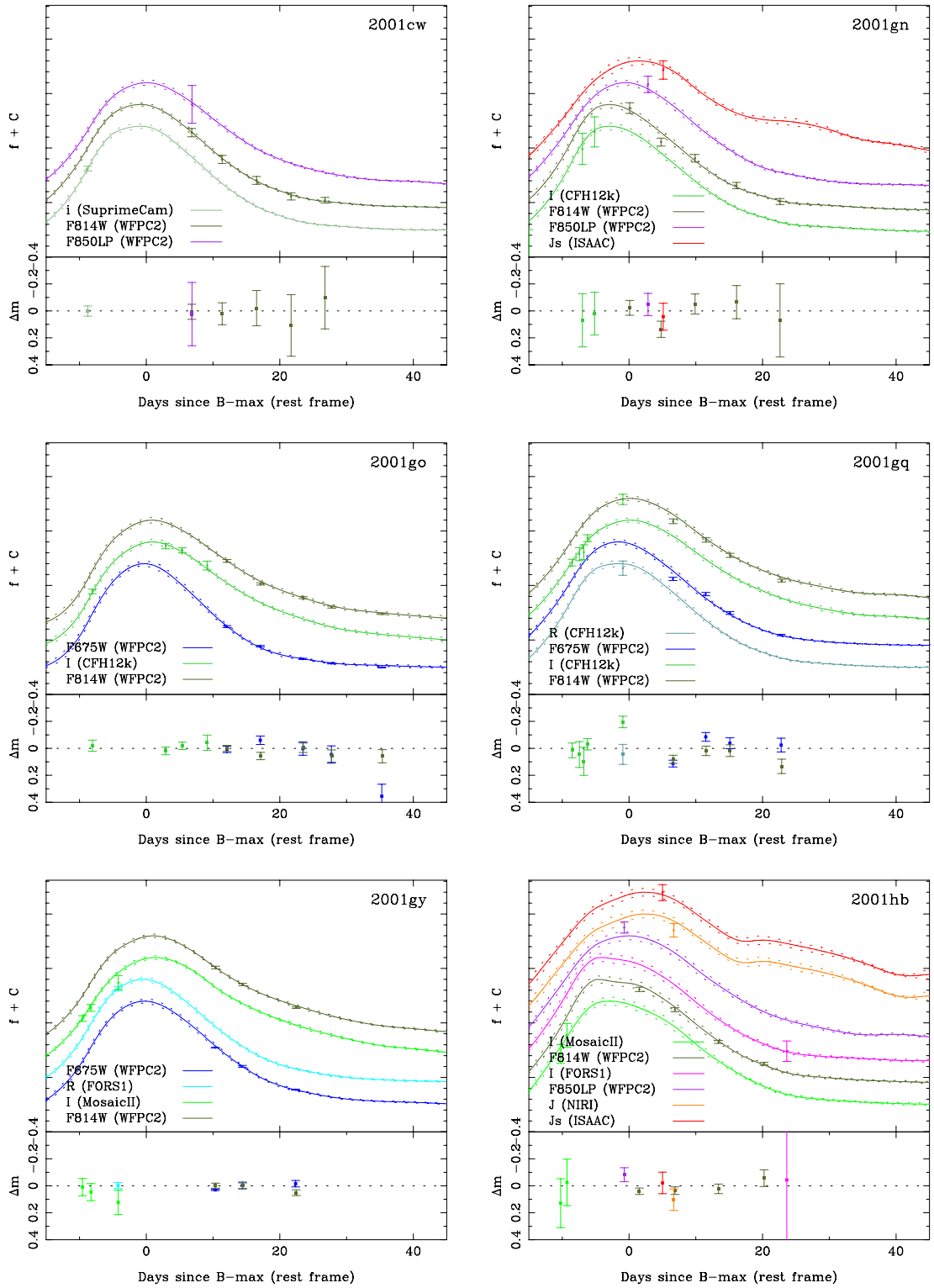

Figure 6. SALT2 light-curve fits together with the data for the six SNe presented here. Light curves for different bands/instruments, indicated by the color coding, have been offset. The dotted lines following the curves represent the model errors.

(A color version of this figure is available in the online journal.)

ing the nonlinearity correction to low flux levels. We have a program (HST GO-11799) to obtain a calibration of NICMOS at low flux levels. The photometry of the SNe observed with NICMOS will be revised once this program is completed. The new data presented in this paper also allow us another route to check this color discrepancy with IR data independent of the NICMOS calibration.

7.2. *Fitting Cosmology*

Following Conley et al. (2006) and K08, we adopt a blind analysis approach for cosmology fitting where the true fitted values are not revealed until the complete analysis framework has been settled. The blind technique is implemented by adjusting the magnitudes of the SNe until they match a fiducial

Table 7
Statistics of Each Sample with No Outlier Rejection or 3σ Outlier Rejection (Used in This Paper)

Set	No Outlier Cut			$\sigma_{\rm cut} = 3$		
	SNe	$\sigma_{\rm sys}(68\%)$	rms (68%)	SNe	$\sigma_{\rm sys}(68\%)$	rms (68%)
Hamuy et al. (1996)	18	$0.15^{+0.05}_{-0.03}$	$0.17^{+0.03}_{-0.03}$	18	$0.15^{+0.05}_{-0.03}$	$0.17^{+0.03}_{-0.03}$
Krisciunas et al. (2005)	6	$0.01^{+0.14}_{-0.01}$	$0.11^{+0.02}_{-0.03}$	6	$0.04^{+0.13}_{-0.04}$	$0.11^{+0.03}_{-0.03}$
Riess et al. (1999)	11	$0.16^{+0.07}_{-0.03}$	$0.17^{+0.03}_{-0.04}$	11	$0.15^{+0.07}_{-0.03}$	$0.17^{+0.03}_{-0.04}$
Jha et al. (2006)	15	$0.20^{+0.07}_{-0.04}$	$0.22^{+0.04}_{-0.04}$	15	$0.21^{+0.07}_{-0.04}$	$0.22^{+0.04}_{-0.04}$
Kowalski et al. (2008)	8	$0.04^{+0.08}_{-0.04}$	$0.14^{+0.03}_{-0.04}$	8	$0.07^{+0.09}_{-0.06}$	$0.15^{+0.03}_{-0.04}$
Hicken et al. (2009b)	104	$0.18^{+0.02}_{-0.02}$	$0.21^{+0.01}_{-0.01}$	102	$0.15^{+0.02}_{-0.01}$	$0.19^{+0.01}_{-0.01}$
Holtzman et al. (2008)	133	$0.19^{+0.02}_{-0.01}$	$0.23^{+0.01}_{-0.01}$	129	$0.10^{+0.01}_{-0.01}$	$0.15^{+0.01}_{-0.01}$
Riess et al. (1998) + HZT	11	$0.31^{+0.19}_{-0.09}$	$0.53^{+0.10}_{-0.12}$	11	$0.31^{+0.19}_{-0.09}$	$0.52^{+0.10}_{-0.12}$
Perlmutter et al. (1999)	33	$0.41^{+0.12}_{-0.09}$	$0.64^{+0.07}_{-0.08}$	33	$0.41^{+0.12}_{-0.09}$	$0.64^{+0.07}_{-0.08}$
Barris et al. (2004)	19	$0.19^{+0.13}_{-0.10}$	$0.39^{+0.06}_{-0.07}$	19	$0.18^{+0.13}_{-0.10}$	$0.38^{+0.06}_{-0.07}$
Amanullah et al. (2008)	5	$0.18^{+0.21}_{-0.06}$	$0.20^{+0.05}_{-0.07}$	5	$0.19^{+0.21}_{-0.06}$	$0.21^{+0.05}_{-0.07}$
Knop et al. (2003)	11	$0.04^{+0.10}_{-0.04}$	$0.15^{+0.03}_{-0.03}$	11	$0.05^{+0.10}_{-0.05}$	$0.15^{+0.03}_{-0.03}$
Astier et al. (2006)	73	$0.18^{+0.03}_{-0.03}$	$0.25^{+0.02}_{-0.02}$	72	$0.13^{+0.03}_{-0.02}$	$0.21^{+0.02}_{-0.02}$
Miknaitis et al. (2007)	77	$0.25^{+0.04}_{-0.03}$	$0.34^{+0.03}_{-0.03}$	74	$0.19^{+0.04}_{-0.03}$	$0.29^{+0.02}_{-0.02}$
Tonry et al. (2003)	6	$0.17^{+0.21}_{-0.10}$	$0.24^{+0.06}_{-0.07}$	6	$0.15^{+0.21}_{-0.12}$	$0.23^{+0.05}_{-0.07}$
Riess et al. (2007)	33	$0.27^{+0.07}_{-0.04}$	$0.49^{+0.06}_{-0.06}$	31	$0.16^{+0.06}_{-0.05}$	$0.45^{+0.05}_{-0.06}$
This paper	6	$0.00^{+0.00}_{0.00}$	$0.12^{+0.03}_{-0.04}$	6	$0.00^{+0.00}_{0.00}$	$0.12^{+0.03}_{-0.04}$
Total	569			557		

Notes. Here, $\sigma_{\rm sys}$ has the same meaning as in Equation (4). Both $\sigma_{\rm sys}$ and the rms are also plotted for each sample in Figure 8. Although each sample is independently fit for its $\sigma_{\rm sys}$ and rms, a global α and β are always used. This explains the minor shifts in parameters for samples where no SNe are cut. A 2σ cut removes 34 more SNe, so going from 3σ to 2σ is consistent with Gaussian residuals.

cosmology ($\Omega_M = 0.25$, $w = -1$). This procedure leaves the residuals only slightly changed, so that the performance of the analysis framework can be studied. The best-fitted cosmology with statistical errors is obtained through an iterative χ^2-minimization of

$$\chi^2_{\rm stat} = \sum_{\rm SNe} \frac{[\mu_B(\alpha, \beta, M) - \mu(z; \Omega_M, \Omega_w, w)]^2}{\sigma^2_{\rm ext} + \sigma^2_{\rm sys} + \sigma^2_{\rm lc}}, \quad (4)$$

where

$$\sigma^2_{\rm lc} = V_{m_B} + \alpha^2 V_{x_1} + \beta^2 V_c + 2\alpha V_{m_B,x_1} - 2\beta V_{m_B,c} - 2\alpha\beta V_{x_1,c} \quad (5)$$

is the propagated error from the covariance matrix, V, of the light-curve fits, with α and β being the x_1 and color correction coefficients of Equation (3). Uncertainties due to host galaxy peculiar velocities of 300 km s^{-1} and uncertainties from Galactic extinction corrections and gravitational lensing as described in Section 7.3 are included in $\sigma_{\rm ext}$. A floating dispersion term, $\sigma_{\rm sys}$, which contains potential sample-dependent systematic errors that have not been accounted for and the observed intrinsic SN Ia dispersion, is also added. The value of $\sigma_{\rm sys}$ is obtained by setting the reduced χ^2 to unity for each sample. Computing a separate $\sigma_{\rm sys}$ for each sample prevents samples with poorer-quality data from increasing the errors of the whole sample. This approach does however still assume that all SNe within a sample are measured with roughly the same accuracy. If this is not the case there is a risk in degrading the constraints from the sample by down weighting the best-measured SNe. It should also be pointed out that the fitted values of $\sigma_{\rm sys}$ will be less certain for small samples and can therefore deviate significantly from the average established by the larger samples (in particular, the six high-z SNe presented in this work are consistent with $\sigma_{\rm sys} = 0$), as are three other samples.

A number of systematic errors are also being considered for the full cosmology analysis. These are taken into account by constructing a covariance matrix for the entire sample which will be described below in Section 7.3. The terms in the denominator of Equation (4) are then added along the diagonal of this covariance matrix.

Following K08, we carry out an iterative χ^2 minimization with 3σ outlier rejection. Each sample is fit for its own absolute magnitude by minimizing the sum of the absolute residuals from its Hubble line (rather than the sum of the squared residuals). The line is then used for outlier rejection. This approach was investigated in detail in K08, and it was shown with simulations that the technique is robust and that the results are unaltered from the Gaussian case in the absence of contamination and that in the presence of a contaminating contribution, its impact is reduced. Table 7 summarizes the effect of the outlier cut on each sample. We also note that the residuals have a similar distribution to a Gaussian in that ~5% of the sample is outside of 2σ.

Figure 7 shows the individual residuals and pulls from the best-fit cosmology together with the fitted SALT2 colors for the different samples. The photometric quality is illustrated by the last column in the figure showing the color uncertainty. It is notable how the photometric quality on the high redshift end has improved from the K08 analysis. This is due to the extended rest-frame range of the SALT2 model compared to SALT.

Figure 8 shows the diagnostics used for studying the consistency between the different samples. The left panel shows the fitted $\sigma_{\rm sys}$ values for each sample together with the rms around the best-fitted cosmology. The intrinsic dispersion associated with all SNe can be determined as the median of $\sigma_{\rm sys}$ as long as the majority of the samples are not dominated by observer-dependent uncertainties that have not been accounted for. The median $\sigma_{\rm sys}$ for this analysis is 0.15 mag, indicated by the

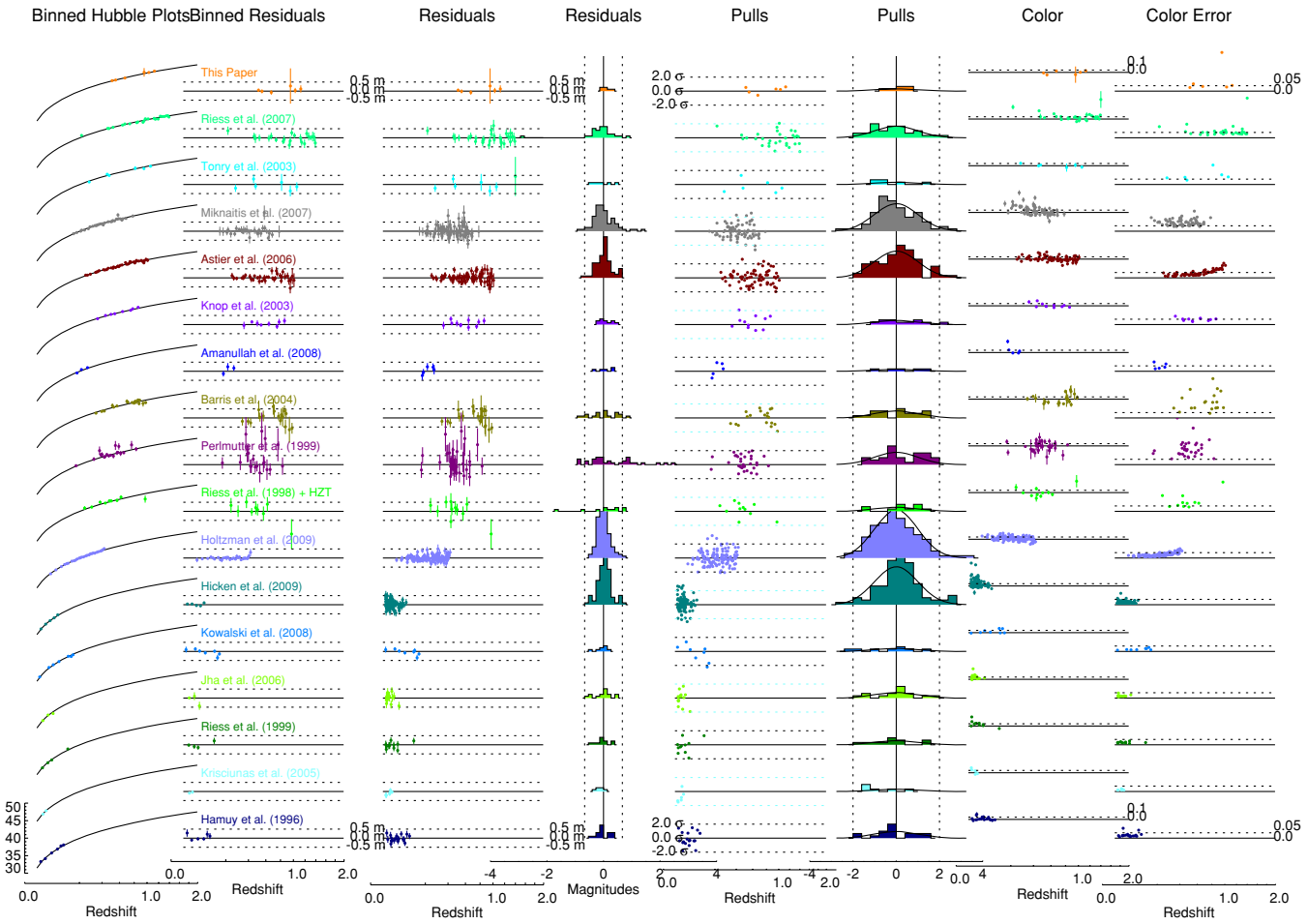

Figure 7. Individual diagrams and distributions for the different data sets. From left to right: (a) Hubble diagrams for the various samples; (b) binned magnitude residuals from the best-fit cosmology (bin-width: $\Delta z = 0.01$); (c) unbinned magnitude residuals from the best fit; (d) histogram of the residuals from the best fit; (e) pull of individual SNe as a function of redshift; (f) histogram of pulls; (g) SN color as a function of redshift; (h) uncertainty of the color measurement as an illustration of the photometric quality of the data.

(A color version of this figure is available in the online journal.)

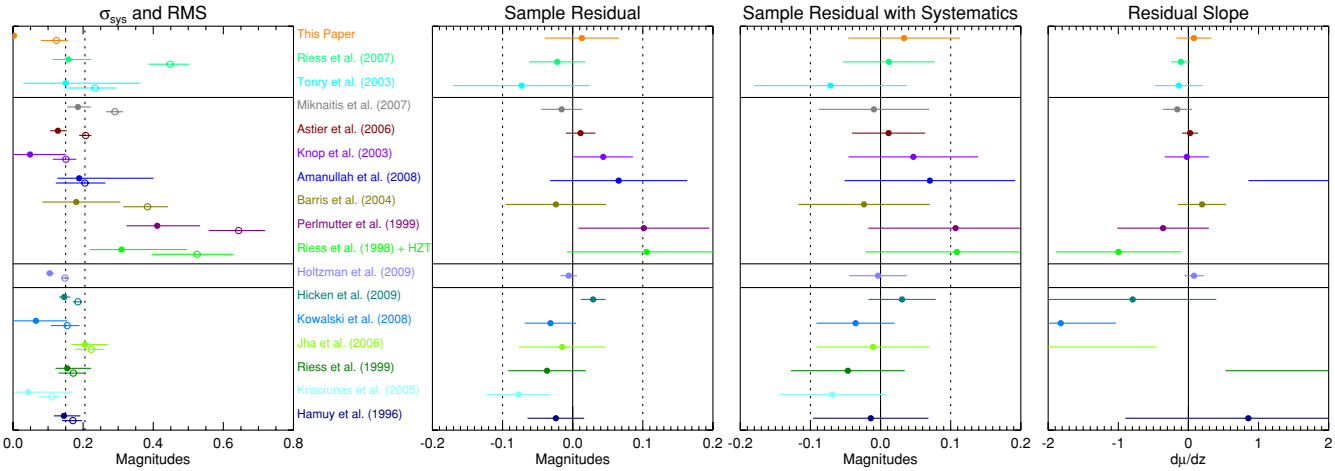

Figure 8. Diagnostics plot for the individual data sets. From left to right: systematic dispersion (filled circles) and rms around the best-fit model (open circles); The mean, sample averaged, deviation from the best-fit model; the slope of the Hubble-residual (in magnitudes) vs. redshift, $d\mu_{\rm residual}/dz$. Note that the errors on the systematic dispersion are the statistical errorbars and do not include possible systematic effects such as misestimating photometry errors.

(A color version of this figure is available in the online journal.)

leftmost dashed vertical line in the figure. The two mid-panels show the tensions for the individual samples, by comparing the average residuals from the best-fit cosmology. The two panels show the tensions without and with systematic errors (described in Section 7.3) being considered. Most samples fall within 1σ and no sample exceeds 2σ. The right panel shows the tension

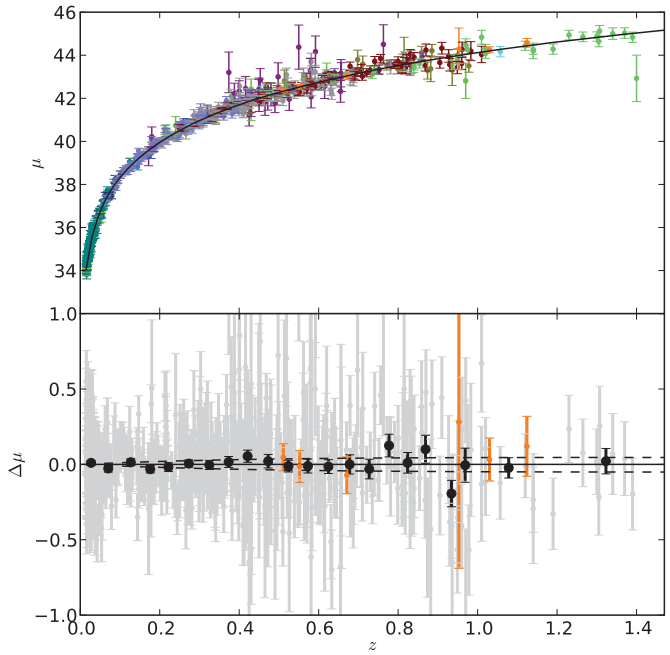

Figure 9. Upper panel: Hubble diagram for the Union2 compilation. The solid line represents the best-fitted cosmology for a flat universe including the CMB and BAO constraints discussed in the text. The different colors have the same interpretation as in Figures 7 and 8. Lower panel: Hubble diagram residuals where the best-fitted cosmology has been subtracted from the light-curve shape and color corrected peak magnitudes. The gray points show the residuals for individual SNe, while the black points show the binned values in redshifts bins of 0.05 for $z < 1.0$ and 0.2 for $z > 1.0$. The orange points show the previously unpublished SNe introduced in this work. The dashed lines show the expected Hubble diagram residuals for cosmological models with $w \pm 0.1$ from the best-fitted value.

(A color version of this figure is available in the online journal.)

of the slopes of the residuals as a function of redshift. This test may not be very meaningful for sparsely sampled data sets, but could reveal possible Malmquist bias for large data sets.

The SNe introduced in this work show no significant tension in any of the panels. The Hubble residuals for these are also presented in Figure 9. Here, the individual SNe are consistent with the best-fit cosmology.

All tables and figures, including the complete covariance matrix for the sample, are available in electronic format on the Union Web page.[34] We also provide a CosmoMC module for including this supernova compilation with other data sets.

7.3. Systematic Errors

The K08 analysis split systematic errors into two categories: the first type affects each SN sample independently, the second type affects SNe at similar redshifts. Malmquist bias and uncertainty in the colors of Vega are examples of the first and second types, respectively. Typical numbers were derived for both of these types of systematics, and they were included as covariances[35] between SNe. Each sample received a common covariance, and all of the high-redshift ($z > 0.2$) SNe shared an additional common covariance.

Other analyses (Astier et al. 2006; Wood-Vasey et al. 2007, KS09) have estimated the effect on w for each systematic error and summed these in the quadrature. However, Kim & Miquel (2006) show that parameterizing systematic errors (such as uncertain zero points) with nuisance parameters is a more appropriate approach and gives better cosmological constraints. For this analysis, all contributing factors, described below, were translated to nuisance parameters, which were then incorporated into a covariance matrix for the distances of the individual SNe. Appendix C contains the details of converting nuisance parameters to a covariance matrix.

Table 8
Assumed Zero-point Uncertainties for SNe in the Union2 Compilation

Source	Band	ZP Uncertainty	Reference
HST	WFPC2	0.02	Heyer et al. (2004)
	ACS	0.03	Bohlin (2007)
	NICMOS	0.03	Thatte et al. (2009)
SNLS	g, r, i	0.01	Astier et al. (2006)
	z	0.03	
ESSENCE	R, I	0.014	Wood-Vasey et al. (2007)
SDSS	u	0.014	Kessler et al. (2009)
	g, r, i	0.009	
	z	0.010	
This paper	R, I	0.03	
	J	0.02	
Other	U band	0.04	Hicken et al. (2009b)
	Other band	0.02	Hicken et al. (2009b)

7.3.1. Zero-point Uncertainties

In order to correctly propagate calibration uncertainties, we computed numerically the effect of each photometric passband on the distance modulus. For each SN, the photometry from each band was shifted in turn by 0.01 mag and then re-fit for μ. We then computed the change in distance modulus, giving $\frac{d\mu(\alpha,\beta)}{d(\mathrm{ZP})}$ for each band. A list of zero-point uncertainties is given in Table 8. For two SNe, i and j, with calibrated photometry obtained in the same photometric system, the zero-point uncertainty, σ_{ZP}, of that system was propagated into the covariance matrix element U_{ij} as $\frac{d\mu_i}{d(\mathrm{ZP})}\frac{d\mu_j}{d(\mathrm{ZP})}\sigma^2_{\mathrm{ZP}}$ according to Appendix C.2.

This procedure is a more efficient way of including zero-point uncertainties than including a common magnitude covariance (multiplicative in flux space) when performing all of the light-curve fits. In testing, both of these methods gave results that agreed at the couple of a percent level. Our method has the advantage that the zero-point errors can be adjusted without rerunning the light curve fits.

Zero-point uncertainties are one of the largest systematic errors (see Table 9). However, we should note that this number is based on a heterogeneous assessment of errors from different data sets (Table 8); the accuracy will vary.

7.3.2. Vega

Astier et al. (2006) estimated the broadband Vega magnitude system uncertainty to be within 1% by comparing spectroscopy from Hayes et al. (1985) and Bohlin & Gilliland (2004). In their analysis, only the uncertainties of Vega colors had implications for cosmological measurements, which they chose to include by adopting a flux uncertainty linear in wavelength that would offset the Vega $B-R$ color by 0.01. The uncertainty of Vega is the single largest source of systematic error when estimating w, as shown in Table 9, suggesting that a better-understood

[34] http://supernova.lbl.gov/Union/

[35] Note that adding a covariance is equivalent to minimizing over a nuisance parameter that has a Gaussian prior around zero; the discussion in K08 is in terms of these nuisance parameters. This is further discussed in Appendix C.

Table 9
Effect on w Errorbar (Including BAO and CMB Constraints) for Each of the Systematic Errors Included

Source	Error on w
Zero point	0.037
Vega	0.042
Galactic extinction normalization	0.012
Rest-frame U-band	0.010
Contamination	0.021
Malmquist bias	0.026
Intergalactic extinction	0.012
Light-curve shape	0.009
Color correction	0.026
Quadrature sum (not used)	0.073
Summed in covariance matrix	0.063

Note. The proper way to sum systematic errors is to include each error in a covariance matrix.

reference would allow for a significant reduction in systematic errors.

KS09, and recently SNLS (Regnault et al. 2009), chose BD+17°4708 as their primary reference star. This star has the advantage of having a well-known SED, measured Landolt magnitudes (in contrast to Vega) and colors that are close to the average colors of the Landolt standards (in contrast to Vega which is much bluer). KS09 studied the implications of switching between BD+17°4708 and Vega and found zero points consistent to ∼1%.

Given this small difference between using BD+17°4708 and Vega, we have chosen, for this work, to continue using Vega as our primary reference star. To account for the uncertainty of the magnitude of Vega on the Landolt system, we have assumed a correlated uncertainty of 0.01 mag for all photometry with a rest-frame wavelength in each of six wavelength intervals defined by the following wavelength boundaries: 2900 Å, 4000 Å, 5000 Å, 6000 Å, 7000 Å, 10000 Å, and 16000 Å.

7.3.3. Rest-frame U Band

SNe Ia are known to show increasing spectroscopic and photometric diversity for wavelengths shorter than the rest-frame B band. Part of this could perhaps be explained by differences in progenitor metallicity (Hoeflich et al. 1998; Lentz et al. 2000), but the spectral variations in the rest-frame UV (Ellis et al. 2008) are larger than predicted by existing models.

As discussed in Section 6, KS09 studied how well the SALT2 model describes the rest-frame U band by first running SALT2 with the rest-frame U band excluded. Using these fits, they then generated a model for the rest-frame U band and binned the magnitude residuals from the actual rest-frame U-band data as a function of phase. For the SDSS and SNLS data sets, the residuals around the time of maximum are ∼3%. For SNLS, this is not surprising, as the SNLS data were used to train the SALT2 model. In this analysis, we use the SDSS sample as a validation set, and include a correlated 0.03 mag uncertainty for all photometric bands bluer than rest-frame 3500 Å.

We note that the *HST* and low-redshift data sets are less useful for assessing the size of rest-frame U-band uncertainty. For the *HST* data, the light curves are poorly constrained without the rest-frame U band. In the case of the nearby sample, the rest-frame U band overlaps with the observed U band for which accurate photometry is generally difficult to obtain (any potential problems with the nearby U band will not impact the light-curve fits much, as the low-z fits are typically very well constrained with the remaining bands).

7.3.4. Malmquist Bias

K08 added a 0.02 mag covariance for each sample representing Malmquist bias uncertainty. More recently, KS09 completed a thorough simulation of selection effects for each of the samples in their analyses. They find a 0.024 change in w when making a correction for selection effects. As the 0.02 mag covariance yields a quite similar 0.026 error on w, and conducting a full simulation is beyond the scope of this work, we reuse the covariance from K08.

7.3.5. Gravitational Lensing

The effects from gravitational lensing on the Hubble diagram have been discussed in detail in the literature (Sasaki 1987; Linder 1988; Bergström et al. 2000; Amanullah et al. 2003; Holz & Linder 2005). Gravitational lensing only affects the high redshift end of the data that is currently available, and potential bias on the cosmological parameters from the analysis carried out here due to the asymmetry of the lensing probability density function is expected to be negligible. We adopt the K08 approach of only treating gravitational lensing as a statistical uncertainty by adding a value of $0.093z$ (Holz & Linder 2005) in quadrature to $\sigma_{\rm ext}$ in Equation (4). This is a conservative approach with respect to the values presented by Jönsson et al. (2006), where they attempt to measure the lensing of individual SNe by determining the mass distribution along the line of sight. A very important conclusion of their work is that there is no evidence for selection effects due to lensing of the high-redshift SNe.

7.3.6. Light-curve Model

We have studied any potential bias that could arise from poor light-curve sampling, by carrying out a similar analysis to K08, updated for SALT2. We use nine *BVR* AQUAA templates (Strovink 2007) constructed from observations of very well-observed nearby SNe. Each set of *BVR* templates is combined with a SALT2 U-band template generated for that supernova, as there were insufficient observations in the U band to construct an AQUAA template.

Mock data sets are then sampled from these templates with the same rest-frame dates and signal-to-noise ratios of the real SNe in our sample. The mock sets are then fitted with SALT2 and the offset between AQUAA corrected magnitude and the corresponding SALT2 fitted value is investigated as a function of the fitted phase of each supernova's first data point (the phase is with respect to B-band maximum). K08 looked at other possible biases, but the first phase was the only significant one found. The test is carried out for each of the nine template SNe.

For SNe with a first phase at B-band maximum, the average bias is close to zero, with an rms of about 0.03. For SNe with a first phase at 6 days past B-band maximum, the average bias is still close to zero, but the rms has increased to about 0.08. Of course, our nine SN templates might not be a representative sample, but these results are encouraging, since they both suggest that there is no significant bias and indirectly validate the SALT2 performance with respect to the AQUAA templates.

We use a first phase cut of 6 days, but we conservatively give each SN that has first phase greater than zero a 0.03 mag covariance. Note that SALT2 does not stretch its definition of phase with light-curve width.

7.3.7. Contamination

As already mentioned, we perform an iterative χ^2 minimization with a 3σ outlier rejection before fitting cosmology. In K08, we showed that this technique greatly reduces the impact of potential contamination, while maintaining roughly Gaussian statistics. Contamination could either come from non-SN Ia or SNe that are typed as normal SN Ia but show peculiarities (see, e.g., Foley et al. 2010).

We carried out a Monte Carlo study showing that the effect of contamination on any individual sample is limited to less than 0.015 mag. This is under the assumption that the dispersion of the contaminating distribution is of the same order, or greater than, the dispersion of SNe Ia and that the contamination is less than 30%. We include a 0.015 mag uncertainty, correlated for each sample, to account for possible contamination.

7.3.8. Minimum Redshift

In order to test for possible effects from using a given minimum redshift cut, we started by constructing a new sample with no minimum redshift. Using this sample, we performed fits which allowed the absolute magnitude to vary independently below and above a dividing redshift in the range 0.01–0.03. This procedure should test for a Hubble bubble or significantly correlated peculiar velocities. The extra degree of freedom allowed by this step in M_B improved the χ^2 by $\lesssim 1$ regardless of the dividing redshift and the inclusion of systematic errors. This confirms the results of Conley et al. (2007) for SALT2. We conclude that there is no statistically significant difference between minimum redshifts and use the value of 0.015, as was used in the K08 analysis.

7.3.9. Galactic Extinction

All light-curve photometry is corrected for Galactic extinction using the extinction law from Cardelli et al. (1989), assuming $R_V = 3.1$, together with the dust maps from Schlegel et al. (1998).

In the same procedure as with calibration uncertainties, we increased the Galactic $E(B-V)$ by 0.01 for each supernova and repeated the fit, giving $\frac{d\mu(\alpha,\beta)}{d(E(B-V))}$. A 16% statistical and 10% systematic error was assumed for the Galactic extinction of each supernova (Schlegel et al. 1998).

7.3.10. Intergalactic Extinction

Dimming of SNe Ia by hypothetical intergalactic gray dust has been suggested by Aguirre (1999) as an alternative to dark energy to explain the SN results (Goobar et al. 2002). This potential dimming was however constrained by studying the colors of high-z quasars (Mörtsell & Goobar 2003; Östman & Mörtsell 2005) and by observations SNe Ia in the rest-frame I band (Nobili et al. 2005, 2009).

Another possible extinction systematic comes from the dust in galaxy halos that are along the line of sight. Ménard et al. (2009b) used distant quasars to detect and measure extinction in galactic halos at $z \sim 0.3$. They find an average R_V for their galaxies of 3.9 ± 2.6. Using their observed $A_V(r)$, we find an average rest-frame V-band extinction of 0.004 mag per intersected halo, assuming $R_V = 3.1$. At redshift 0.5, an average of three halos has been intercepted. At redshift 1.0, the average is 7.

There are three mitigating factors. One is that expansion redshifts photons between the supernova and the intervening galaxy. The CCM law decreases with wavelength (in the relevant wavelength range), so less light is absorbed. Ménard et al. (2008) find that $\rho_{\rm dust} \propto (1+z)^{-1.1}$, which we use to scale the extinction. Finally, most of the extinction is corrected by color correction. The exact amount corrected depends on the redshift and the filters used in the observations, but is around two-thirds.

We find an error on w of 0.008 due to this extinction, significantly lower than the value of 0.024 derived by Ménard et al. (2009a). However, they used $R_V = 3.9$, rather than 3.1; the fraction of extinction that is corrected by the color correction will decrease with R_V. We also numerically sum the CCM laws, rather than using an analytic approximation. Since we know the exact redshift and filters used in each observation, we can exactly calculate the amount of extinction already handled by the color correction (using our $\frac{d\mu}{dzp}$ values), without approximation.

7.3.11. Shape and Color Correction

The most uncertain contribution to the dimming of SNe Ia is host galaxy extinction. Several studies of SN Ia colors (Guy et al. 2005, 2007; Wang et al. 2008; Nobili & Goobar 2008, and references therein) indicate that the observed SN Ia reddening does not match the Galactic CCM extinction law with $R_V = 3.1$. A stronger wavelength dependence has been found in the optical in most cases, and it remains unclear if CCM models with any value of R_V can be used to describe the data accurately. It is possible that the observed steep reddening originates from a mixture of local effects and host galaxy extinction. Local effects could be intrinsic SN variations, but also multiple scattering on dust in the circumstellar environment has been suggested (Wang 2005; Goobar 2008). This model is potentially supported by detection (Patat et al. 2007; Simon et al. 2009; Blondin et al. 2009) of circumstellar material but also by color excess measurements for two of the best-observed reddened SN Ia (Folatelli et al. 2010) being consistent with the expected extinction from circumstellar material.

The SALT2 method approaches the lack of a consistent understanding of SN Ia reddening by adopting a purely empirical approach. For SALT2, the SN Ia luminosity is standardized by assuming that the standardization is linear in both x_1 and c as described in Equation (3), where β is the empirically determined correction coefficient that accounts for all linear relations between color and observed peak magnitude. For example, if the only source for such SN Ia reddening originated from CCM extinction then β is identically equal to $R_V + 1$. We test this approach and propagate relevant systematic uncertainties by dividing the full sample into smaller sets and carrying out independent fits for the x_1 and c correction coefficients, α and β, as shown in Table 10.

When subdividing into redshift bins, we find that the values of α and β for the full sample are consistent with values for the three first redshift bins. It is encouraging to see consistency between the global values fit for the full data set and the values in the best-understood redshift range. Beyond this important test, we also note that the value of β in the redshift range 0.5–1 is significantly lower than the other values, while the value for $z > 1$ is higher than the global value, but is poorly measured. The trend is similar to what was seen in KS09, but we use different binning. This behavior is inconsistent with a monotonic drift in redshift, so we consider other explanations for these results. That conclusion is also supported by the observation that samples at similar redshifts (e.g., Miknaitis et al. 2007; Astier et al. 2006) can have very different values of β when fitted independently. The value of α is consistent across redshift ranges, except at $z > 1$, where many light curves are so poorly sampled that it may not be possible to assign reasonable x_1 errors.

Table 10
Subdivisions of the Union2 Compilation

Cut	Number	M_B	α	β	Ω_M	w
$0.015 \leqslant z \leqslant 0.10$	166	$-19.323^{+0.016}_{-0.016}$	$0.112^{+0.011}_{-0.011}$	$2.77^{+0.09}_{-0.09}$	0.270 (fixed)	−1.000 (fixed)
$0.100 \leqslant z \leqslant 0.25$	74	$-19.326^{+0.020}_{-0.020}$	$0.154^{+0.019}_{-0.018}$	$2.49^{+0.15}_{-0.14}$	0.270 (fixed)	−1.000 (fixed)
$0.250 \leqslant z \leqslant 0.50$	154	$-19.305^{+0.014}_{-0.014}$	$0.110^{+0.013}_{-0.013}$	$2.50^{+0.12}_{-0.11}$	0.270 (fixed)	−1.000 (fixed)
$0.500 \leqslant z \leqslant 1.00$	133	$-19.309^{+0.016}_{-0.017}$	$0.129^{+0.018}_{-0.018}$	$1.45^{+0.19}_{-0.19}$	0.270 (fixed)	−1.000 (fixed)
$z \geqslant 1.000$	16	$-19.450^{+0.083}_{-0.106}$	$-0.124^{+0.085}_{-0.118}$	$3.84^{+1.20}_{-0.85}$	0.270 (fixed)	−1.000 (fixed)
$c \geqslant 0.05$	245	$-19.373^{+0.026}_{-0.026}$	$0.112^{+0.011}_{-0.011}$	$2.96^{+0.10}_{-0.10}$	$0.283^{+0.017}_{-0.016}$	$-0.969^{+0.070}_{-0.074}$
$c \leqslant 0.05$	308	$-19.305^{+0.019}_{-0.020}$	$0.122^{+0.010}_{-0.010}$	$1.13^{+0.30}_{-0.28}$	$0.284^{+0.015}_{-0.015}$	$-0.959^{+0.058}_{-0.062}$
$x_1 \geqslant -0.25$	302	$-19.358^{+0.023}_{-0.023}$	$0.026^{+0.021}_{-0.021}$	$2.60^{+0.10}_{-0.09}$	$0.278^{+0.015}_{-0.014}$	$-0.996^{+0.061}_{-0.065}$
$x_1 \leqslant -0.25$	254	$-19.335^{+0.031}_{-0.032}$	$0.147^{+0.020}_{-0.019}$	$2.42^{+0.10}_{-0.10}$	$0.276^{+0.016}_{-0.015}$	$-1.016^{+0.069}_{-0.073}$
Holtzman et al. (2008)	129	$-19.315^{+0.013}_{-0.013}$	$0.147^{+0.014}_{-0.013}$	$2.38^{+0.15}_{-0.14}$	0.270 (fixed)	−1.000 (fixed)
Hicken et al. (2009b)	102	$-19.299^{+0.021}_{-0.022}$	$0.113^{+0.013}_{-0.013}$	$2.73^{+0.10}_{-0.10}$	0.270 (fixed)	−1.000 (fixed)
Miknaitis et al. (2007)	74	$-19.325^{+0.032}_{-0.033}$	$0.112^{+0.037}_{-0.035}$	$2.50^{+0.17}_{-0.16}$	0.270 (fixed)	−1.000 (fixed)
Astier et al. (2006)	71	$-19.287^{+0.016}_{-0.017}$	$0.140^{+0.017}_{-0.017}$	$1.72^{+0.18}_{-0.17}$	0.270 (fixed)	−1.000 (fixed)
$z \geqslant 0.015$	557	$-19.310^{+0.014}_{-0.014}$	$0.121^{+0.007}_{-0.007}$	$2.51^{+0.07}_{-0.07}$	$0.277^{+0.014}_{-0.014}$	$-1.009^{+0.050}_{-0.054}$

Notes. Values of absolute B-band magnitude, M_B (assuming $H_0 = 70$ km s^{-1} Mpc^{-1}), as well as stretch and color correction coefficients, α and β, for several redshift ranges. Ω_M and w are shown for properly conducted x_1 and c cuts, chosen to give similar uncertainty of the fitted w. The outlier rejection is re-done for each bin, so the totals may not add up to the whole sample. The constraints are computed including BAO and CMB data.

When subdividing into the four largest data sources (the lower half of Table 10), we find values of α and β generally consistent with the global values, with the exception of a lower value of β for the SNLS SNe (Astier et al. 2006). In general, ignoring or underestimating the errors in c or x_1 will decrease the associated correction coefficients, β and α, as investigated in K08 and KS09 and this may be relevant here. Specifically, two potential sources of problems are an incomplete understanding of calibration and underestimated SN model variations, either of which could affect these fits. If the SNLS SNe are physically different, and they are allowed their own β, then w shifts by 0.02. Alternatively, as one β is used for the global sample, the possibility that β is biased from the true global value must be considered. Selecting the global value of β from any of the other large samples shifts w by less than 0.02. We have accounted for this systematic by assigning each sample a 0.02 mag covariance (giving a 0.03 error on w), which avoids the problem of handling an error on elements of the covariance matrix. To study these details further, we look forward to more data for $z > 0.5$, with improved calibration and light-curve models.

We also perform one additional sanity check by subdividing the data by x_1 and c. There is evidence for two populations of normal SN Ia, divided by light-curve width (see K08, and references therein). Star-forming galaxies tend to host the population with broader light curves, while SN hosted by passive galaxies tends to have narrower light curves. As described below, we derive consistent cosmology for these subdivisions as well.

We subdivide[36] the full sample into two roughly equal subsamples, split first by color and then by x_1. In total, this makes four subsamples. We find that the cosmology is close for all subsamples (as can be seen in Table 10) so the difference from these subdivisions does not contribute significantly to the systematic error on w.

It is interesting to note that α is substantially different for the two samples split by light-curve width. Likewise, β is substantially different for the two samples split by color. This might suggest that the relationships between color and brightness and light curve width and brightness are more complex than a simple linear relationship, or it could be that the errors on x_1 and c are not perfectly understood. We also find that β is higher for the redder SNe Ia which is similar to the results from Conley et al. (2008) based on comparisons of $U-B$ colors to $B-V$, after correcting for the effect of stretch on the U band. At the same time, it should be pointed out that evidence of low R_V values has also been found for a few well-studied, and significantly reddened, nearby SNe Ia (Folatelli et al. 2010).

7.3.12. Summary of Systematic Errors

The effect of these systematic errors on w is given in Table 9. The improvement in cosmology constraints over the simple quadrature sum is also shown. Zero-point and Vega calibration dominate the systematics budget, but understanding the color variations of SNe is also important. The benefit from making a Malmquist bias correction can be seen; by doing so, KS09 reduce this systematic error by a factor of 2.

8. RESULTS AND DISCUSSION

The best-fit cosmological parameters for the compilation are presented in Table 11 with constraints from CMB and BAO. The confidence regions in the (Ω_M, Ω_Λ) and (Ω_M, w) planes for the last fit in the table are shown in Figures 10 and 11, respectively.

In the cosmology analysis presented here, the statistical errors on Ω_M have decreased by a significant 24% over the K08 Union analysis, while the estimated systematic errors have only improved by 13%. When combining the SN results with BAO and CMB constraints, statistical errors on w have improved

[36] Subdividing by x_1 or c must be done carefully. When there are errors in both the dependent and independent variables (in this case, magnitude and x_1 or c), the true values of the independent variables must be explicitly solved for as part of the fit. Otherwise, the subdividing will be biased. For example, suppose that a supernova has a color that is poorly measured, and an uncorrected magnitude that is well measured. If this supernova is faint and blue, then a fit for the true color will give a redder color. A color cut will place this supernova in the blue category, when the supernova is actually more likely to be red. As mentioned in K08, whenever one fits for α and β, the true values of x_1 and c are only implicitly solved for; Equation (5) is derived by analytically minimizing over the true x_1 and c. K08 provides the equation with the true values being made explicit, we also include a discussion in Appendix C.

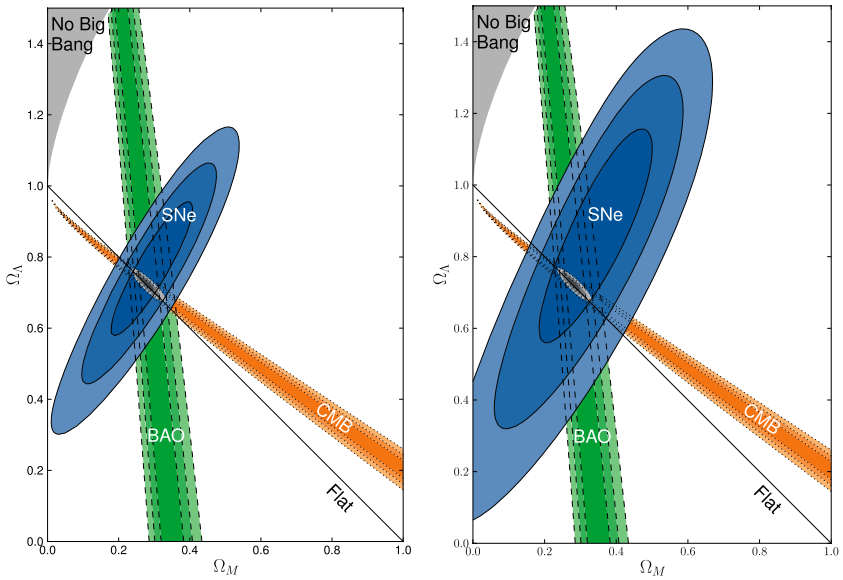

Figure 10. 68.3%, 95.4%, and 99.7% confidence regions in the $(\Omega_M, \Omega_\Lambda)$ plane from SNe combined with the constraints from BAO and CMB both without (left panel) and with (right panel) systematic errors. Cosmological constant dark energy ($w = -1$) has been assumed.
(A color version of this figure is available in the online journal.)

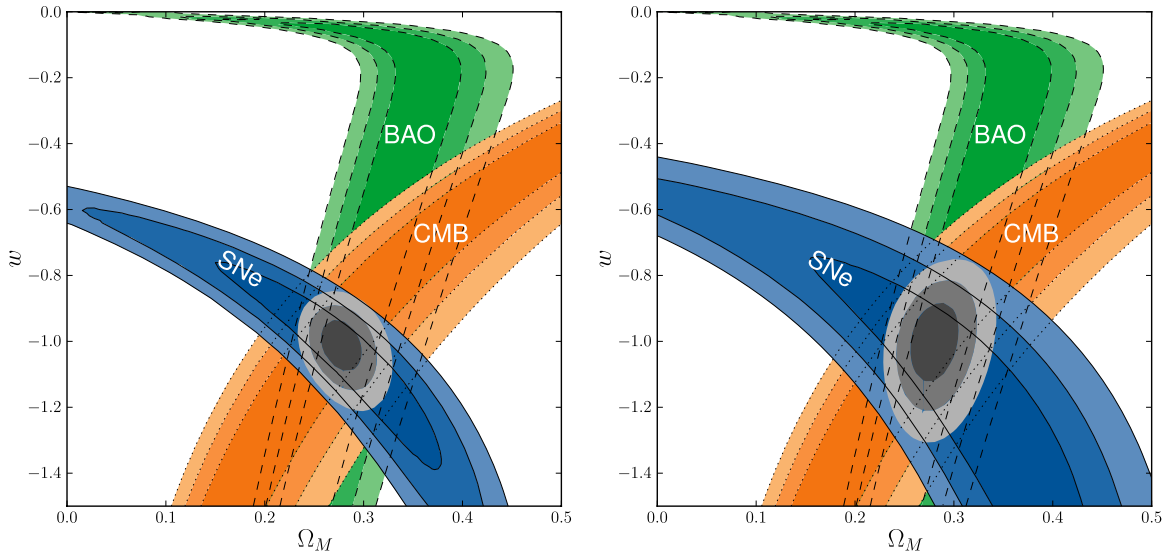

Figure 11. 68.3%, 95.4%, and 99.7% confidence regions of the (Ω_M, w) plane from SNe combined with the constraints from BAO and CMB both without (left panel) and with (right panel) systematic errors. Zero curvature and constant w have been assumed.
(A color version of this figure is available in the online journal.)

by 16% over K08, though the quoted systematic errors have increased by 7%. Figure 12 shows a comparison between the constraints from K08 and this compilation in the $(\Omega_M$–$w)$ plane. Even with some improvement on the understanding of systematic errors, it is clear that the data set is dominated by systematic error (at least at low- to mid-z).

For the CMB data we implement the constraints from the seven year data release of the *Wilkinson Microwave Anisotropy Probe* (*WMAP*) as outlined in Komatsu et al. (2010). We take their results on $z_\star$ (the redshift of last scattering), $l_A(z_\star)$, and $R(z_\star)$, updating the central values for the cosmological model being considered. Here, $l_A(z_\star)$ is given by

$$l_A(z_\star) \equiv (1 + z_\star)\frac{\pi D_A(z_\star)}{r_s(z_\star)},$$

where D_A is the angular distance to $z_\star$, while

$$R(z_\star) \equiv \frac{\sqrt{\Omega_M H_0^2}}{c}(1 + z_\star)D_A(z_\star).$$

Percival et al. (2010) measure the position of the BAO peak from the SDSS DR7 and 2dFGRS data, constraining $d_z \equiv r_s(z_d)/D_V(0.275)$ to 0.1390 ± 0.0037, where $r_z(z_d)$ is the comoving sound horizon and $D_V(z) \equiv \left[(1 + z)^2 D_A^2 cz/H(z)\right]^{1/3}$.

For the SNe + BAO fit in Table 11, we add an H_0 measurement of 74.2 ± 3.6 km s^{-1} Mpc^{-1} from Riess et al. (2009), creating a constraint without the CMB that is therefore largely independent of the high-redshift behavior of dark energy (as long as the dark energy density contribution is negligible in the early universe). Note that the H_0 constraint relies on most of the nearby SNe used in this compilation. However, the effect on w through H_0

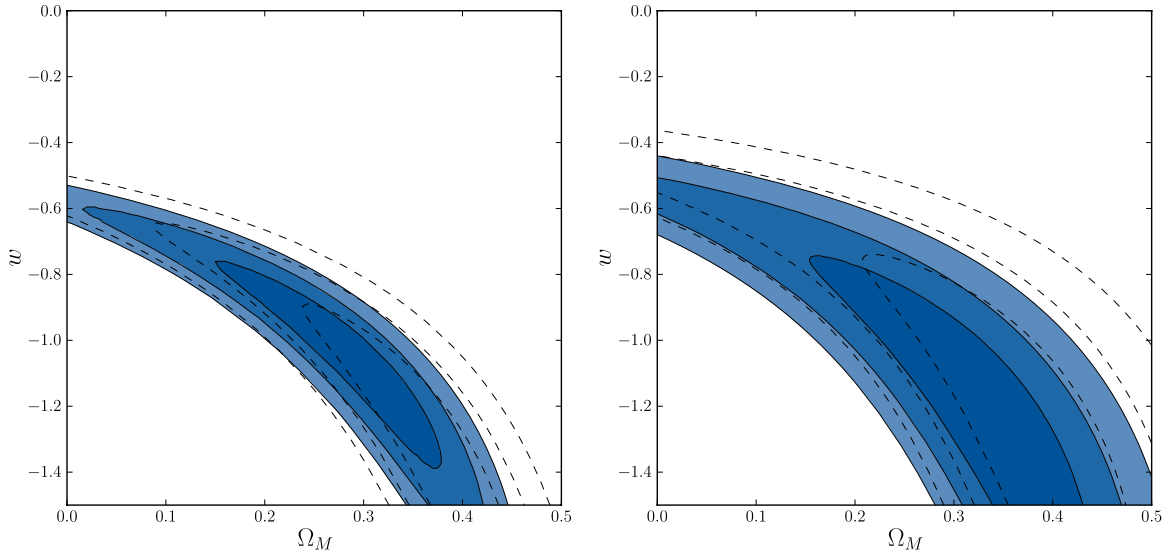

Figure 12. 68.3%, 95.4%, and 99.7% confidence regions of the (Ω_M, w) plane from SNe alone from K08 (dashed contours) and this compilation (shaded contours). Systematic errors are included in the right panel. Zero curvature has been assumed.
(A color version of this figure is available in the online journal.)

Table 11
Fit Results on Cosmological Parameters Ω_M, w, and Ω_k

Fit	Ω_M	Ω_M w/Sys	Ω_k	Ω_k w/Sys	w	w w/Sys
SNe	$0.270^{+0.021}_{-0.021}$	$0.274^{+0.040}_{-0.037}$	0 (fixed)	0 (fixed)	−1 (fixed)	−1 (fixed)
SNe+BAO+H_0	$0.309^{+0.032}_{-0.032}$	$0.316^{+0.036}_{-0.035}$	0 (fixed)	0 (fixed)	$-1.114^{+0.098}_{-0.112}$	$-1.154^{+0.131}_{-0.150}$
SNe+CMB	$0.268^{+0.019}_{-0.017}$	$0.269^{+0.023}_{-0.022}$	0 (fixed)	0 (fixed)	$-0.997^{+0.050}_{-0.055}$	$-0.999^{+0.074}_{-0.079}$
SNe+BAO+CMB	$0.277^{+0.014}_{-0.014}$	$0.279^{+0.017}_{-0.016}$	0 (fixed)	0 (fixed)	$-1.009^{+0.050}_{-0.054}$	$-0.997^{+0.077}_{-0.082}$
SNe+BAO+CMB	$0.278^{+0.014}_{-0.014}$	$0.282^{+0.018}_{-0.016}$	$-0.003^{+0.006}_{-0.006}$	$-0.004^{+0.006}_{-0.007}$	−1 (fixed)	−1 (fixed)
SNe+BAO+CMB	$0.281^{+0.016}_{-0.015}$	$0.282^{+0.018}_{-0.016}$	$-0.004^{+0.007}_{-0.007}$	$-0.005^{+0.008}_{-0.007}$	$-1.029^{+0.056}_{-0.059}$	$-1.038^{+0.093}_{-0.097}$
SNe+BAO+CMB+H_0	$0.275^{+0.015}_{-0.014}$	$0.274^{+0.016}_{-0.015}$	$-0.001^{+0.006}_{-0.006}$	$-0.002^{+0.007}_{-0.007}$	$-1.024^{+0.055}_{-0.058}$	$-1.052^{+0.092}_{-0.096}$

Note. The parameter values are followed by their statistical (first column) and statistical and systematic (second column) uncertainties.

from these SNe is several times smaller than the effect through the Hubble diagram. Alternatively, adding a CMB constraint on $\Omega_m h^2$ of 0.1338 ± 0.0058 from the *WMAP7* Web page[37] allows us to create a constraint that is independent of H_0. This final result for SNe+BAO+CMB does not improve significantly if the current H_0 constraint is added.

8.1. Time Variation of the Dark Energy Equation of State

The constraints shown in Figure 11 were obtained assuming that the dark energy EOS is redshift independent. SNe Ia are useful for constraining a redshift dependent $w(z)$ since, unlike e.g., CMB, their measured distances at a given redshift are independent of the behavior of dark energy at higher redshifts. A common method to parameterize $w(z)$ is

$$w(z) = w_0 + w_a \frac{z}{1+z},$$

where a cosmological constant is described by $(w_0, w_a) = (-1, 0)$. It can be shown (Linder 2003) that this parameterization provides an excellent approximation to a wide variety of dark energy models. The constraints from the current SN data together with the CMB and BAO data are presented in Figure 13.

In terms of the figure of merit,[38] introduced by the dark energy task force (Albrecht et al. 2006), these constraints correspond to 1.2 and 1.8 with and without systematics, respectively. The flattening of the contours in this diagram at $w_0 + w_a = 0$ comes from the implicit constraint of matter domination in the early universe imposed by the CMB and BAO data. Only modest constraints can currently be placed on w_a.

It can be illuminating to study $w(z)$ in redshift bins, where w is assumed constant in each bin. This method has the advantage that $w(z)$ can be studied without assuming a specific form for the relation (Huterer & Starkman 2003). We carry out the analysis following Kowalski et al. (2008) and fit a constant w in each bin, while the remaining cosmological parameters are fit globally for the entire redshift range. Figure 14 shows three such models for the combined constraints from SNe, BAO, CMB, and H_0 measurements where we assume a flat universe. In these scenarios, the H_0 measurement does not contribute much, but due to its small improvement on the CMB constraints it gives a small (∼10%) improvement on the errorbar of the highest redshift bin.

The left panel shows constraints on w for three bins. The first bin ($0 < z < 0.5$) shows a well-constrained w. The middle bin ($0.5 < z < 1$) shows a poorly constrained w, though one

[37] http://lambda.gsfc.nasa.gov/product/map/current/params/wcdm_sz_lens_wmap7.cfm

[38] Defined as the inverse area of the joint 2σ region in the Gaussian limit ($\Delta\chi^2 = 6.17$).

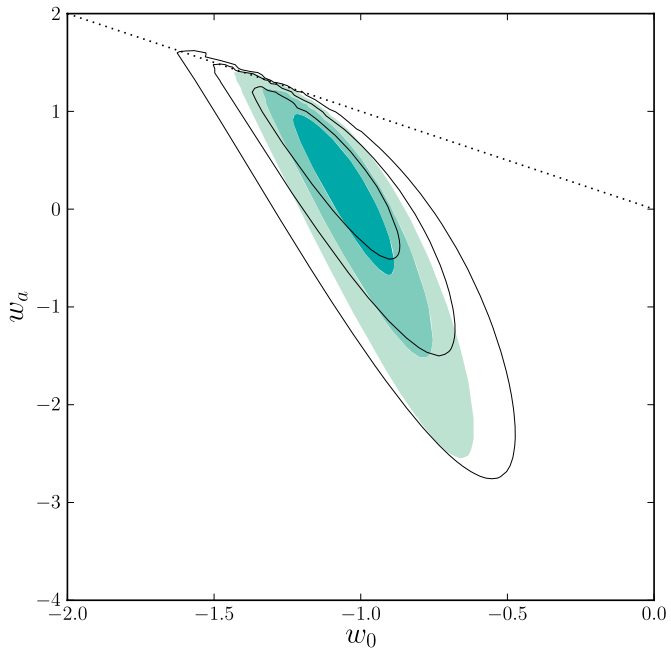

Figure 13. 68.3%, 95.4%, and 99.7% confidence regions of the (w_0, w_a) plane from SNe combined with the constraints from BAO and CMB both with (solid contours) and without (shaded contours) systematic errors. Zero curvature has been assumed. Points above the dotted line ($w_0 + w_a = 0$) violate early matter domination and are implicitly disfavored in this analysis by the CMB and BAO data.

(A color version of this figure is available in the online journal.)

that is distinct from $-\infty$ (which would drive ρ to 0 above $z = 0.5$, resulting in a matter-only universe) at high confidence, indicating the detection of some kind of dark energy in this redshift range. For $z > 1$, there is little constraint on w and only a weak constraint on the existence of dark energy.

The middle panel shows the effect of dividing the highest redshift bin. The constraints on w for $z > 1$ get much weaker, showing that most of the (weak) constraint on the highest bin in the left panel comes from a combination of the CMB with the well-constrained low-redshift supernova data. Current SNe at $z > 1$ offer no real constraint on $w(z > 1)$. Providing a significant constraint at these redshifts requires significantly better supernova measurements. As in the left panel, w in the highest redshift bin is constrained to be less than zero by the requirement from BAO and CMB constraints that the early universe has a matter-dominated epoch.

The right panel shows the effect of dividing the lowest redshift bin. While no significant change in w with redshift is detected, there is still considerable room for evolution in w, even at low redshift.

Figure 15 shows dark energy *density* constraints, assuming the same redshift binning as in Figure 14. Note that this is not equivalent to the left and center panels of Figure 14; only in the limit of an infinite number of bins do binned ρ and binned w give the same model. Dark energy can be detected at high significance in the middle bin (redshift 0.5–1), but there is only weak evidence for dark energy above redshift 1 (left panel). When the bin above redshift 1 is split at a redshift greater than the supernova sample (right panel), it can be seen that the current small sample of SNe cannot constrain the existence of dark energy above redshift 1.

8.2. SNe with Ground-based Near-IR Data

Obtaining near-IR data of $z \gtrsim 1$ SNe Ia, whether from space or from the ground, is critical for constraining the SALT2 color parameter, c. Without the near-IR data, the uncertainty in this parameter for 2001hb and 2001gn, both beyond $z = 1$, increases by a factor of 2. Precise measurements of c are important, since uncertainties in c are inflated by $\beta \approx 2.5$ and tend to dominate the error budget when the corrected peak B-brightness of SNe Ia is calculated.

Both 2001hb and 2001gn were observed with ground-based near-IR instruments. The operational challenges associated in obtaining these data are significant. Long exposure times (10 hr or more taken within a few days) in excellent observing conditions are necessary. Even with queue mode scheduling, these observations are just feasible. Despite the challenges, the uncertainty in the SALT2 color of these two SNe Ia is comparable to the uncertainty in the color of the *best* space-based measured SNe Ia at $z \gtrsim 1$.

The ground-based near-IR data also allow us to search for systematic offsets with near-IR data taken from space. For $z > 1.1$ SNe Ia observed with NICMOS, the average SALT2 c value is $c = 0.06 \pm 0.03$ mag. By comparison, the weighted average color of the three SNe Ia at $z \sim 1.1$ with ground-based near-IR data (2001hb and 2001gn from this

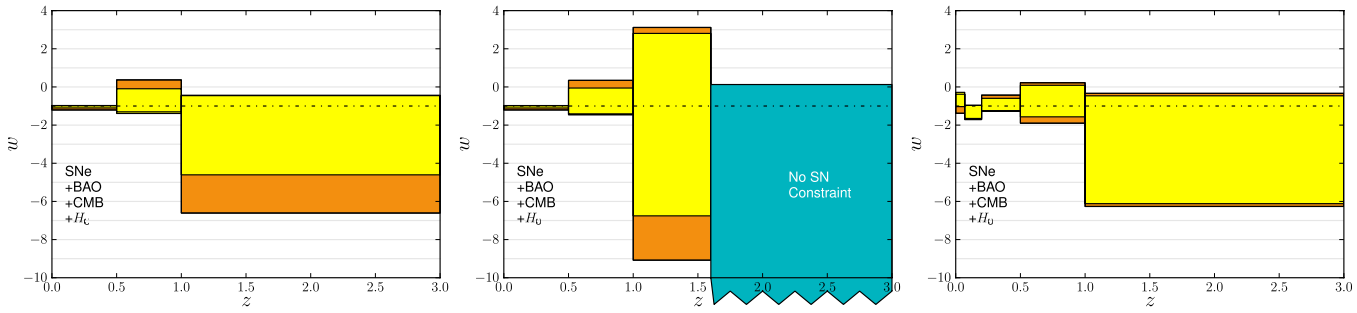

Figure 14. Constraints on $w(z)$, where $w(z)$ is assumed to be constant in each redshift bin, are plotted at the 68% probability level. The results were obtained assuming a flat universe for the joint data set of SNe, BAO, CMB, and H_0, with (dark/orange) and without (light/yellow) SN systematics. The left panel shows three redshift bins, with the highest redshift bin keeping w constant for all $z > 1$. Dark energy is seen to exist at $z > 1$ (at least at 68% cl) since w does not reach an infinitely negative value, indicating its density does not go to zero. The middle panel splits this last bin into two, showing that the seemingly tight constraints on dark energy at $z > 1$ with current data depend on the combination of CMB with low-redshift data. No current probe alone can constrain the existence of dark energy at $z > 1$. The right panel shows the effects of w binning at low redshift. The best-fit values of w go from less than -1 at $z = 0.14$ to greater than -1 at $z = 0.04$. While such a steep, late time transition in w (corresponding to $dw/d\ln a \approx 7$) is unusual in physical models, it can easily appear due to offsets between heterogeneous data sets. We emphasize that the results are still consistent with the cosmological constant (dot-dashed line) at the 68% confidence level.

(A color version of this figure is available in the online journal.)

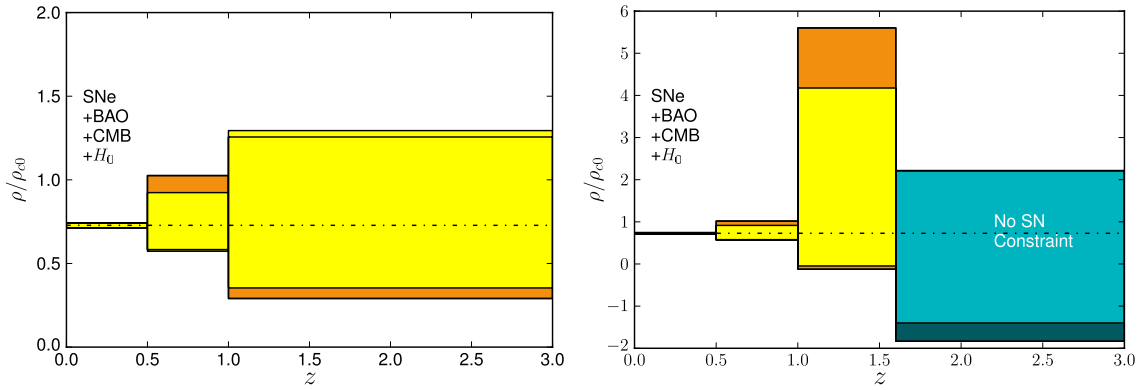

Figure 15. Dark energy density in units of the critical density today, ρ/ρ_{c0}, is assumed constant in each bin. The same binning as the left/center panels in Figure 14 is chosen. As can be seen in the left panel, dark energy is detected between redshift 0.5 and 1 at high significance, but only hints of dark energy are seen above redshift 1. When the CMB and SNe are separated, neither one alone can provide any evidence for dark energy at $z > 1$.

(A color version of this figure is available in the online journal.)

work, together with 1999fk from Tonry et al. 2003) that pass the light-curve cuts is, 0.01 ± 0.07. Neither the ground-based or space-based measurements show any Hubble diagram offset ($\Delta\mu = 0.03 \pm 0.10$ and -0.01 ± 0.06, respectively) from the best-fit cosmology. These results include a 0.1 mag dispersion in color, and the fitted systematic dispersions in magnitude. Additional SNe Ia at $z \sim 1.1$ with ground-based near-IR photometry will be published in N. Suzuki et al. (2010, in preparation) and we will revisit this issue in that paper, where we will also incorporate the results from the NICMOS calibration program referenced in Section 7.1.

8.3. Comparison of KeplerCam and SDSS Photometry

H09 and KS09 share three normal SNe in common: 2005hc, 2005hj, and 2005ir. In comparing the data for these SNe, we noticed that the H09 KeplerCam *r*-band photometry is generally 0.05 ± 0.02 mag fainter than the KS09 SDSS *r*-band photometry based on SALT2 fits including both data sets. The quoted uncertainty is completely dominated by the zero-point uncertainties, as both sets of data have high S/N. The offset is consistent for each supernova. This offset is the correct size and direction to explain the tension in Hubble residuals seen between these data sets in the second panel of Figure 8.

SN 2005hc and SN 2005ir were also observed by CSP using the Swope telescope. In these cases, the Swope photometry agrees with the SDSS *r*-band photometry.

9. SUMMARY AND CONCLUSIONS

We have presented the light curves of SNe Ia in the redshift range $0.511 < z < 1.12$. The SNe were discovered as part of a search conducted by the SCP using the Subaru, CFHT, and CTIO Blanco telescopes in 2001. The fitted light-curve shapes and colors at maximum light are all consistent with the corresponding distributions from previous SN surveys.

Following K08, we add these six SNe and other SN Ia data sets to the Union compilation. We have also improved the Union analysis in a number of respects, creating the new Union2 compilation. The most important improvements are (1) systematic errors are directly computed using the effect they have on the distance modulus and (2) all SN light curves are fitted with the SALT2 light-curve fitter.

We determine the best-fit cosmology for the Union2 compilation, and the concordance ΛCDM model remains an excellent fit. The new analysis results in a significant improvement over K08 in constraining w over the redshift interval $0 < z < 1$. Above $z \gtrsim 1$, evidence for dark energy is weak. This will remain the case until there is much more high redshift data, with better signal-to-noise and wavelength coverage.

Based, in part, on observations obtained at the ESO La Silla Paranal Observatory (ESO programs 67.A-0361 and 169.A-0382). Based, in part, on observations obtained at the CTIO, National Optical Astronomy Observatory, which are operated by the Association of Universities for Research in Astronomy, under contract with the National Science Foundation. Based, in part, on observations obtained at the Gemini Observatory (Gemini programs GN-2001A-SV-19 and GN-2002A-Q-31), which is operated by the Association of Universities for Research in Astronomy, Inc., under a cooperative agreement with the NSF on behalf of the Gemini partnership: the National Science Foundation (USA), the Particle Physics and Astronomy Research Council (UK), the National Research Council (Canada), CONICYT (Chile), the Australian Research Council (Australia), CNPq (Brazil), and CONICET (Argentina). Based, in part on observations obtained at the Subaru Telescope, which is operated by the National Observatory of Japan. Some of imaging data taken with Suprime-Cam were obtained during the commissioning phase of the instrument, and we thank all members of Suprime-Cam instrument team. Based, in part, on data that were obtained at the W. M. Keck Observatory, which is operated as a scientific partnership among the California Institute of Technology, the University of California and the National Aeronautics and Space Administration. The Observatory was made possible by the generous financial support of the W. M. Keck Foundation. Based on observations obtained at the CFHT which is operated by the National Research Council of Canada, the Institut National des Sciences de l'Univers of the Centre National de la Recherche Scientifique of France, and the University of Hawaii. The authors recognize and acknowledge the very significant cultural role and reverence that the summit of Mauna Kea has always had within the indigenous Hawaiian community. We are most fortunate to have the opportunity to conduct observations from this mountain.

Based, in part, on observations made with the NASA/ESA *Hubble Space Telescope*, obtained at the STScI, which is operated by the Association of Universities for Research in

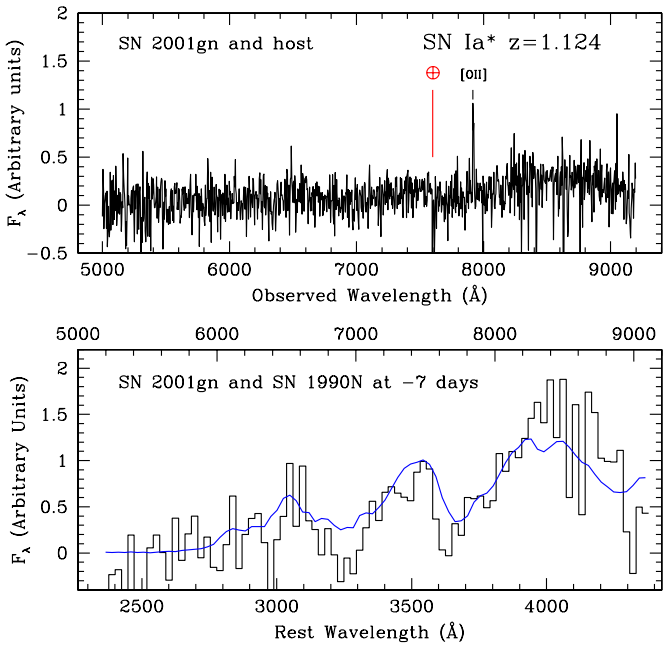

Figure A1. Upper panel: the error weighted and rebinned ESI spectrum of 2001gn, a probable SN Ia at $z = 1.124$. The redshift is derived from the [O II] λλ3727, 3729 doublet, which is clearly resolved in the ESI spectrum. Lower panel: the rebinned host galaxy subtracted spectrum and SN 1990N at −7 days.

(A color version of this figure is available in the online journal.)

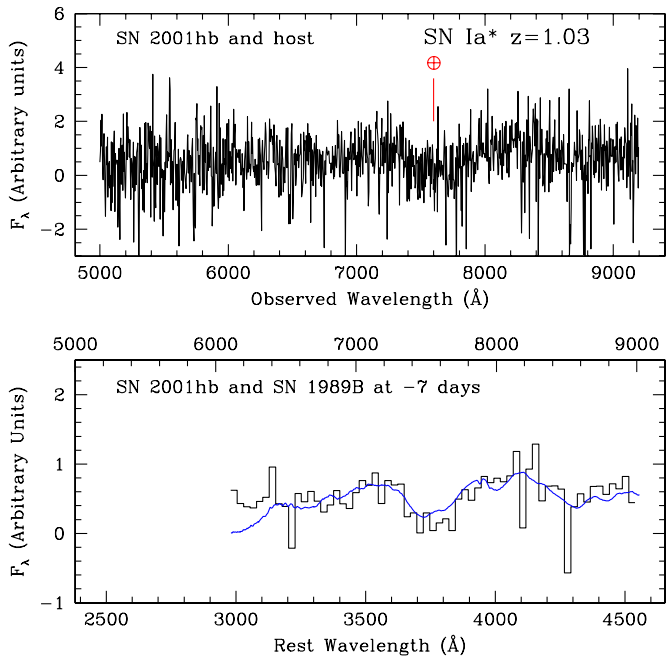

Figure A2. Upper panel: the error-weighted and rebinned ESI spectrum of 2001hb, a probable SN Ia at $z = 1.03$. Lower panel: a rebinned version of the spectrum in the upper panel and SN 1989B at −7 days. The redshift of 2001hb is derived by fitting the SN to local SN templates as no features from the host galaxy are detected.

(A color version of this figure is available in the online journal.)

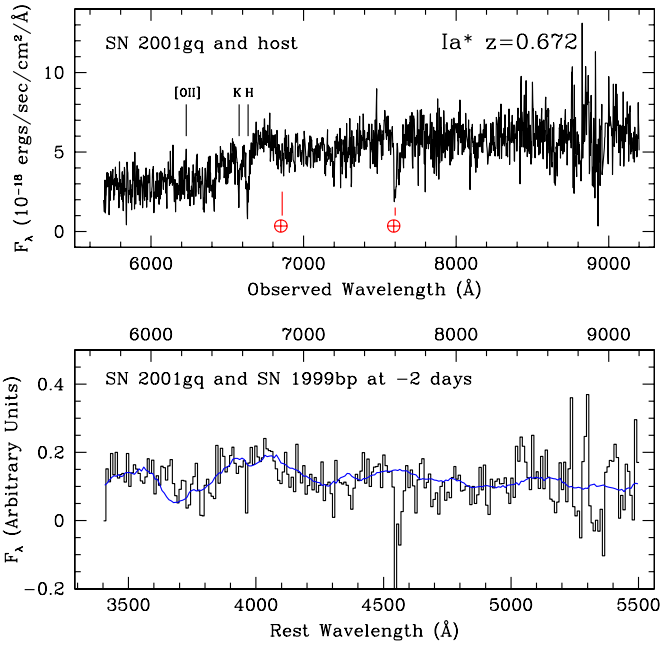

Figure A3. Upper panel: the unbinned LRIS spectrum of 2001gq, a probable SN Ia at $z = 0.672$. Lower panel: the rebinned host galaxy subtracted spectrum and SN 1999bp at −2 days.

(A color version of this figure is available in the online journal.)

Astronomy, Inc., under NASA contract NAS 5-26555. These observations are associated with programs HST-GO-08585 and HST-GO-09075.

Support for programs HST-GO-08585.14-A and HST-GO-09075.01-A was provided by NASA through a grant from the STScI, which is operated by the Association of Universities for Research in Astronomy, Inc., under NASA contract NAS 5-26555.

This work is supported in part by a Japan Society for the Promotion of Science (JSPS) core-to-core program "International Research Network for Dark Energy" and by JSPS research grants (20040002).

This work was supported by the Director, Office of Science, Office of High Energy Physics, of the U.S. Department of Energy under Contract No. DE- AC02-05CH11231.

T.M. is financially supported by the JSPS through the JSPS Research Fellowship. C.L. acknowledges the support provided by the Oskar Klein Centre at Stockholm University. The authors thank the anonymous referee for helpful comments and suggestions.

Facilities: HST (WFPC2,ACS), Keck:I (LRIS), Keck:II (ESI), CFHT (CFH12k), Gemini:Gillett (NIRI), Subaru (SuprimeCam), Blanco (MOSAIC II), NTT (SuSI2), VLT:Antu (FORS1,ISAAC)

APPENDIX A

SPECTRA AND NOTES ON INDIVIDUAL CANDIDATES

The spectra of six SNe are presented in this paper. Details of the spectra for 2001go and 2001gy can be found in Lidman et al. (2005), while the spectrum for 2001cw is described in Morokuma et al. (2010).

The spectrum of each candidate is plotted twice (see Figures A1–A3). In the upper panel, the spectrum of the candidate is plotted in the observer frame and is uncorrected for host galaxy light. Telluric absorption features are marked with the symbol ⊕. In the lower panel, contamination from the host (if any) is removed, and the resulting spectrum is rescaled and rebinned. This spectrum is plotted in black as a histogram and it is plotted in both the rest frame (lower axis) and the observer frame (upper axis). For comparison, low redshift SNe are plotted as a blue continuous line.

Table B1
Follow-up Photometry of the Six SNe Presented in This Paper

SN	MJD	Instrument	Exp.	Band	Flux	ZP	I.Q.
2001cw	52024.43	SuprimeCam	3600	*i*	1.6E + 00 (5.0E − 01)	27.30 (0.03)	1.05
2001cw	52049.50	SuprimeCam	3240	*i*	1.3E + 01 (4.6E − 01)	27.30 (0.03)	1.47
2001cw	52079.88	WFPC2	2300	*F814W*	8.3E − 01 (4.3E − 02)	23.72 (0.02)	0.10
2001cw	52079.94	WFPC2	2400	*F850LP*	2.1E − 01 (4.5E − 02)	22.03 (0.02)	0.10
2001cw	52088.77	WFPC2	2300	*F814W*	5.6E − 01 (4.2E − 02)	23.72 (0.02)	0.10
2001cw	52098.81	WFPC2	2300	*F814W*	3.4E − 01 (4.1E − 02)	23.72 (0.02)	0.10
2001cw	52108.91	WFPC2	2300	*F814W*	1.8E − 01 (3.7E − 02)	23.72 (0.02)	0.10
2001cw	52118.81	WFPC2	4400	*F814W*	1.4E − 01 (2.9E − 02)	23.72 (0.02)	0.10

Notes. The columns list the SN name, the weighted average MJD of the observation, exposure time, filter pass band, measured flux, instrumental ZP, and image quality in arc seconds. The ZPs are in the Landolt systems, and the instrumental magnitude, m, is obtained as $m = -2.5 \log_{10} f + \mathrm{ZP}$, where f can be obtained from the flux column.
(This table is available in its entirety in a machine-readable form in the online journal. A portion is shown here for guidance regarding its form and content.)

Table B2
All SNe Included in This Compilation

SN	z_{CMB}	$m_B^{\max}$	x_1	c	μ	Sample	Cut
1993ah	0.0285	16.86(0.19)	−2.26(0.93)	0.23(0.09)	34.61(0.23)	1	...
1993ag	0.0500	17.79(0.05)	−1.09(0.24)	0.12(0.02)	35.95(0.17)	1	...
1993o	0.0529	17.60(0.05)	−1.03(0.14)	−0.01(0.02)	36.09(0.16)	1	...
1993b	0.0701	18.43(0.04)	−0.53(0.21)	0.09(0.02)	36.71(0.16)	1	...
1992bs	0.0627	18.25(0.05)	−0.27(0.23)	0.02(0.02)	36.75(0.16)	1	...
1992br	0.0876	19.19(0.11)	−2.97(0.38)	−0.04(0.07)	37.50(0.19)	1	...
1992bp	0.0786	18.27(0.04)	−1.27(0.20)	−0.02(0.02)	36.76(0.16)	1	...
1992bo	0.0172	15.75(0.13)	−2.68(0.18)	0.03(0.02)	33.93(0.20)	1	...
1992bl	0.0422	17.30(0.08)	−1.95(0.24)	0.02(0.04)	35.61(0.17)	1	...
1992bh	0.0453	17.58(0.05)	−0.02(0.25)	0.10(0.02)	35.91(0.17)	1	...

Notes. The columns represent the SN name, redshift, peak B-band magnitude, SALT2 parameters x_1 and c, distance modulus, sample and failed cuts (if any). z: redshift < 0.015; o: outlier; d: number of observations < 5; f: bad light-curve fit; p: first phase greater than 6 days after B-band maximum.
References. (1) Hamuy et al. 1996; (2) Krisciunas et al. 2005; (3) Riess et al. 1999; (4) Jha et al. 2006; (5) Kowalski et al. 2008; (6) Hicken et al. 2009b; (7) Holtzman et al. 2008; (8) Schmidt et al. 1998, + HZT; (9) Perlmutter et al. 1999; (10) Barris et al. 2004; (11) Amanullah et al. 2008; (12) Knop et al. 2003; (13) Astier et al. 2006; (14) Miknaitis et al. 2007; (15) Tonry et al. 2003; (16) Riess et al. 2007; (17) this paper.
(This table is available in its entirety in a machine-readable form in the online journal. A portion is shown here for guidance regarding its form and content.)

APPENDIX B

LIGHT-CURVE DATA

Tabulated below are light-curve data for the six SNe presented in this paper. The data are listed in chronological order for one SN at a time and correspond to data points plotted in Figure 6.

All photometry is given as the measured flux, f, in the instrumental system, i.e., no color correction (S-correction) to a standard system has been applied. The instrumental Vega magnitude may be calculated using the standard formula: $m = -2.5 \log f + \mathrm{ZP}$, where ZP is the associated zero point. For the *HST* data these are the updated values from Dolphin (2000) given on Andrew Dolphin's Web page.[39] The zero points have then been converted to e/s by using a gain of 7.12. The zero points for the ground-based data on the other hand are always given for the photometric reference image, and therefore include exposure time, gain, and for the PSF fitted data, the aperture correction. Note that there are correlated errors between the data points that come from the same light-curve build, since the same host galaxy model and zero point have been used. This is also reflected by small offsets between different data sets in Figure 6. The covariances are taken into account for the light-curve fitting and the full covariance matrices used will be available from the SCP Web site.

The instruments used are as given below. MOSAIC II is the multichip imager on the CTIO 4 m telescope. CFH12k is the multichip imager on the 3.6 m CFHT telescope on Mauna Kea in Hawaii. SuprimeCamis the wide-field imager on the 8.2 m Subaru telescope. SuSI2is the imager on the NTT 3.6 m telescope at ESO. FORS1 is the imager on the 8 m UT2 (Kueyen) at VLT, ESO. ISAAC and NIRI are the near-infrared imagers on the 8 m UT1 (Antu) at VLT, ESO, and Gemini North telescopes, respectively. Finally, WFPC2 indicates data obtained with the PC CCD and ACS is the Advanced Camera for Surveys, both on *HST*.

[39] http://purcell.as.arizona.edu/wfpc2_calib/

APPENDIX C

NUISANCE PARAMETERS AS COVARIANCES

Suppose that observations $\boldsymbol{y}$ are modeled by $\boldsymbol{F}(\boldsymbol{\theta})$, where some of the parameters enter into the model linearly ($\boldsymbol{\theta}^L$) while some enter nonlinearly ($\boldsymbol{\theta}^N$). The χ^2 can be written as

$$\chi^2(\boldsymbol{\theta}) = (\boldsymbol{y} - (\boldsymbol{F}_N(\boldsymbol{\theta}^N) + H\boldsymbol{\theta}^L))^T V^{-1} (\boldsymbol{y} - (\boldsymbol{F}_N(\boldsymbol{\theta}^N) + H\boldsymbol{\theta}^L)), \quad \text{(C1)}$$

where V is the covariance matrix of the observations and H is the Jacobian matrix of the model with respect to the $\boldsymbol{\theta}^L$. Taking the derivative of the χ^2 and setting it to zero gives the analytic formula for the best-fit $\boldsymbol{\theta}^L$

$$\hat{\boldsymbol{\theta}^L} = (H^T V^{-1} H)^{-1} H^T V^{-1} (\boldsymbol{y} - \boldsymbol{F}_N(\boldsymbol{\theta}^N)) \equiv D(\boldsymbol{y} - \boldsymbol{F}_N(\boldsymbol{\theta}^N)). \tag{C2}$$

The likelihoods for the $\boldsymbol{\theta}^N$ can be found from this restricted parameter space where $\boldsymbol{\theta}^L = \hat{\boldsymbol{\theta}^L}$. Thus, the restricted χ^2 is given by

$$\chi^2 = ((I - HD)(\boldsymbol{y} - \boldsymbol{F}_N(\boldsymbol{\theta}^N)))^T V^{-1} \times (I - HD)(\boldsymbol{y} - \boldsymbol{F}_N(\boldsymbol{\theta}^N)) \tag{C3}$$

$$\equiv (\boldsymbol{y} - \boldsymbol{F}_N(\boldsymbol{\theta}^N))^T U^{-1} (\boldsymbol{y} - \boldsymbol{F}_N(\boldsymbol{\theta}^N)) \tag{C4}$$

with U^{-1} given by

$$U^{-1} = (I - HD)^T V^{-1} (I - HD) \tag{C5}$$

$$= V^{-1} - V^{-1} H (H^T V^{-1} H)^{-1} H^T V^{-1}. \tag{C6}$$

In this way, all of the $\boldsymbol{\theta}^L$ do not have to be explicitly included in the χ^2, as long as the weight matrix, U^{-1}, is updated appropriately. Note that U^{-1} may depend on $\boldsymbol{\theta}^N$.

C.1. Minimization Over $x_1^{\rm true}$ and $c^{\rm true}$

When errors in the independent variable are present, the true values must be solved for as part of the fit (see discussion in K08). For one supernova, $\boldsymbol{y} = (m_B, x_1, c)$, while the model is given by

$$\left(M_B + \mu(z, \text{cosmology}) - (\alpha x_1^{\rm true} - \beta c^{\rm true}), x_1^{\rm true}, c^{\rm true}\right). \tag{C7}$$

Using $\boldsymbol{\theta}^L = (x_1^{\rm true}, c^{\rm true})$ (M_B, α and β are global parameters and cannot be handled one supernova at a time), we have

$$H = \begin{pmatrix} -\alpha & \beta \\ 1 & 0 \\ 0 & 1 \end{pmatrix}. \tag{C8}$$

The new χ^2 for this specific example (equation (C4)) is given by Equations (4) and (5).

C.2. Minimization Over Systematic Errors

Suppose that we have two kinds of measurements: supernova distance measurements (N SNe) and zero-point measurements (M zero points). The true value of each zero point is given by $\text{ZP}_{\rm true} = \text{ZP}_{\rm observed} + \Delta\text{ZP}$. Because the uncertainties on the supernova distances are unrelated to the uncertainties on the zero points,

$$V = \begin{pmatrix} V_\mu & \\ & V_{\Delta\text{ZP}} \end{pmatrix},$$

where V_μ is an $N \times N$ block and $V_{\Delta\text{ZP}}$ is an $M \times M$ block. Similarly, $\boldsymbol{y}$ can be split into distances and zero points $\boldsymbol{y} = (\boldsymbol{y}_\mu, \boldsymbol{y}_{\Delta\text{ZP}} = \boldsymbol{0})$. The model for each supernova distance is given by

$$M_B + \mu(z, \text{cosmology}) - \sum_\lambda \frac{\partial(m_B + \alpha x_1 - \beta c)}{\partial \text{ZP}_\lambda} \Delta\text{ZP}_\lambda. \tag{C9}$$

It is derived in the same way as in the previous section, with the substitutions $x_1 \rightarrow x_1 + \sum_\lambda \frac{\partial x_1}{\partial \text{ZP}_\lambda} \Delta\text{ZP}_\lambda$ and $c \rightarrow c + \sum_\lambda \frac{\partial c}{\partial \text{ZP}_\lambda} \Delta\text{ZP}_\lambda$. The model for the true offset of each zero point is simply ΔZP. Thus,

$$H = \begin{pmatrix} H_\mu \\ I \end{pmatrix}.$$

The upper block of U^{-1} is given by

$$U^{-1}_{\text{upper block}} = V_\mu^{-1} - V_\mu^{-1} H_\mu \left(V_{\Delta\text{ZP}}^{-1} + H_\mu^T V_\mu^{-1} H_\mu\right)^{-1} H_\mu^T V_\mu^{-1}; \tag{C10}$$

none of the other blocks enter into the χ^2. Inverting this block (see Hager 1989) gives

$$U = V_\mu + H_\mu V_{\Delta\text{ZP}} H_\mu^T. \tag{C11}$$

Equation (C11) gives us the terms we must add to the supernova distance modulus errors to correctly take the zero points into account.

REFERENCES

Adelman-McCarthy, J. K., et al. 2007, ApJS, 172, 634
Aguirre, A. 1999, ApJ, 525, 583
Alard, C. 2000, A&AS, 144, 363
Alard, C., & Lupton, R. H. 1998, ApJ, 503, 325
Albrecht, A., et al. 2006, arXiv:astro-ph/0609591
Amanullah, R., Mörtsell, E., & Goobar, A. 2003, A&A, 397, 819
Amanullah, R., et al. 2008, A&A, 486, 375
Anderson, J., & King, I. R. 2003, PASP, 115, 113
Appenzeller, I., et al. 1998, Messenger, 94, 1
Astier, P., et al. 2006, A&A, 447, 31
Barris, B. J., et al. 2004, ApJ, 602, 571
Bergström, L., Goliath, M., Goobar, A., & Mörtsell, E. 2000, A&A, 358, 13
Bessell, M. S. 1990, PASP, 102, 1181
Blondin, S., Prieto, J. L., Patat, F., Challis, P., Hicken, M., Kirshner, R. P., Matheson, T., & Modjaz, M. 2009, ApJ, 693, 207
Bohlin, R. C. 2007, in ASP Conf. Ser. 364, The Future of Photometric, Spectrophotometric and Polarimetric Standardization, ed. C. Sterken (San Francisco, CA: ASP), 315
Bohlin, R. C. 2007, Photometric Calibration of the ACS CCD Cameras, ACS Instrument Science Report 2007-06 (Baltimore, MD: STScI)
Bohlin, R. C., & Gilliland, R. L. 2004, AJ, 127, 3508
Cardelli, J. A., Clayton, G. C., & Mathis, J. S. 1989, ApJ, 345, 245
Conley, A., Carlberg, R. G., Guy, J., Howell, D. A., Jha, S., Riess, A. G., & Sullivan, M. 2007, ApJ, 664, L13
Conley, A., et al. 2006, ApJ, 644, 1
Conley, A., et al. 2008, ApJ, 681, 482
Copin, Y., et al. 2006, New Astron. Rev., 50, 436
Cuillandre, J.-C., Luppino, G., Starr, B., & Isani, S. 2000, Astron. Telescopes Instrum., 4008, 1010
Dawson, K. S., et al. 2009, AJ, 138, 1271
D'Odorico, S., Beletic, J. W., Amico, P., Hook, I., Marconi, G., & Pedichini, F. 1998, Proc. SPIE, 3355, 507
Dolphin, A. E. 2000, PASP, 112, 1397
Dolphin, A. E. 2009, PASP, 121, 655
Eisenstein, D. J., et al. 2005, ApJ, 633, 560
Ellis, R. S., et al. 2008, ApJ, 674, 51
Fabbro, S. 2001, PhD thesis, l'Université Paris XI Orsay
Filippenko, A. V., Li, W. D., Treffers, R. R., & Modjaz, M. 2001, in ASP Conf. Ser. 246, IAU Colloq. 183: Small Telescope Astronomy on Global Scales, ed. B. Paczynski, W.-P. Chen, & C. Lemme (San Francisco, CA: ASP), 121
Folatelli, G., et al. 2010, AJ, 139, 120
Foley, R. J., Narayan, G., Challis, P. J., Filippenko, A. V., Kirshner, R. P., Silverman, J. M., & Steele, T. N. 2010, ApJ, 708, 1748
Foley, R. J., et al. 2008, ApJ, 684, 68
Fruchter, A. S., & Hook, R. N. 2002, PASP, 114, 144
Fukugita, M., Ichikawa, T., Gunn, J. E., Doi, M., Shimasaku, K., & Schneider, D. P. 1996, AJ, 111, 1748
Garnavich, P. M., et al. 1998, ApJ, 509, 74
Goldhaber, G., et al. 2001, ApJ, 558, 359

Goobar, A. 2008, ApJ, 686, L103
Goobar, A., Bergström, L., & Mörtsell, E. 2002, A&A, 384, 1
Guy, J., Astier, P., Nobili, S., Regnault, N., & Pain, R. 2005, A&A, 443, 781
Guy, J., et al. 2007, A&A, 466, 11
Hager, W. W. 1989, SIAM Rev., 31, 221
Hamuy, M., Phillips, M. M., Suntzeff, N. B., Schommer, R. A., Maza, J., & Aviles, R. 1996, AJ, 112, 2398
Hamuy, M., et al. 2006, PASP, 118, 2
Hayes, D. S., Pasinetti, L. E., & Philip, A. G. D. (ed.) 1985, IAU Symp. 111, Calibration of Fundamental Stellar Quantities (Dordrecht: Reidel)
Heyer, I., Richardson, M., Whitmore, B., & Lubin, L. 2004, The Accuracy of WFPC2 Photometric Zeropoints, Instrument Science Report WFPC2 2004-001 (Baltimore, MD: STScI)
Hicken, M., Wood-Vasey, W. M., Blondin, S., Challis, P., Jha, S., Kelly, P. L., Rest, A., & Kirshner, R. P. 2009a, ApJ, 700, 1097
Hicken, M., et al. 2009b, ApJ, 700, 331
Hodapp, K. W., et al. 2003, PASP, 115, 1388
Hoeflich, P., Wheeler, J. C., & Thielemann, F. K. 1998, ApJ, 495, 617
Holtzman, J. A., et al. 2008, AJ, 136, 2306
Holz, D. E., & Linder, E. V. 2005, ApJ, 631, 678
Hook, I. M., et al. 2005, AJ, 130, 2788
Howell, D. A., Sullivan, M., Conley, A., & Carlberg, R. 2007, ApJ, 667, L37
Howell, D. A., et al. 2005, ApJ, 634, 1190
Huterer, D., & Starkman, G. 2003, Phys. Rev. Lett., 90, 031301
James, F., & Roos, M. 1975, Comput. Phys. Commun., 10, 343
Jha, S., Riess, A. G., & Kirshner, R. P. 2007, ApJ, 659, 122
Jha, S., et al. 2006, AJ, 131, 527
Jönsson, J., Dahlén, T., Goobar, A., Gunnarsson, C., Mörtsell, E., & Lee, K. 2006, ApJ, 639, 991
Kessler, R., et al. 2009, ApJS, 185, 32
Kim, A. G., & Miquel, R. 2006, Astropart. Phys., 24, 451
Knop, R. A., et al. 2003, ApJ, 598, 102
Komatsu, E., et al. 2010, arXiv:1001.4538
Kowalski, M., et al. 2008, ApJ, 686, 749
Krisciunas, K., et al. 2005, AJ, 130, 2453
Krist, J. E., & Hook, R. N. 2001, The Tiny Tim User's Guide (Baltimore, MD: STScI)
Kuznetsova, N., et al. 2008, ApJ, 673, 981
Landolt, A. U. 1992, AJ, 104, 340
Law, N. M., et al. 2009, PASP, 121, 1395
Lentz, E. J., Baron, E., Branch, D., Hauschildt, P. H., & Nugent, P. E. 2000, ApJ, 530, 966
Lidman, C., et al. 2005, A&A, 430, 843
Linder, E. V. 1988, A&A, 206, 190
Linder, E. V. 2003, Phys. Rev. Lett., 90, 091301
Lupton, R. 2005, Transformations between SDSS Magnitudes and UBVRcIc, http://www.sdss.org/dr6/algorithms/sdssUBVRITransform.html#Lupton2005
Ménard, B., Kilbinger, M., & Scranton, R. 2009a, arXiv:0903.4199
Ménard, B., Nestor, D., Turnshek, D., Quider, A., Richards, G., Chelouche, D., & Rao, S. 2008, MNRAS, 385, 1053
Ménard, B., Scranton, R., Fukugita, M., & Richards, G. 2009b, arXiv:0902.4240
Miknaitis, G., et al. 2007, ApJ, 666, 674
Miyazaki, S., et al. 2002, PASJ, 54, 833
Moorwood, A., et al. 1998, The Messenger, 94, 7
Morokuma, T., et al. 2010, PASJ, 62, 19
Mörtsell, E., & Goobar, A. 2003, J. Cosmol. Astropart. Phys., JCAP04(2003)003
Muller, G. P., Reed, R., Armandroff, T., Boroson, T. A., & Jacoby, G. H. 1998, Proc. SPIE, 3355, 577
Nobili, S., & Goobar, A. 2008, A&A, 487, 19
Nobili, S., et al. 2005, A&A, 437, 789
Nobili, S., et al. 2009, ApJ, 700, 1415
Nugent, P., Kim, A., & Perlmutter, S. 2002, PASP, 114, 803
Oke, J. B., et al. 1995, PASP, 107, 375
Östman, L., & Mörtsell, E. 2005, J. Cosmol. Astropart. Phys., JCAP02(2005)005
Patat, F., et al. 2007, Science, 317, 924
Percival, W. J., et al. 2010, MNRAS, 401, 2148
Perlmutter, S., et al. 1995, ApJ, 440, L41
Perlmutter, S., et al. 1997, ApJ, 483, 565
Perlmutter, S., et al. 1998, Nature, 391, 51
Perlmutter, S., et al. 1999, ApJ, 517, 565
Persson, S. E., Murphy, D. C., Krzeminski, W., Roth, M., & Rieke, M. J. 1998, AJ, 116, 2475
Phillips, M. M. 1993, ApJ, 413, L105
Raux, J. 2003, PhD thesis, l'Université Paris XI Orsay
Regnault, N., et al. 2009, A&A, 506, 999
Riess, A. G., Press, W. H., & Kirshner, R. P. 1996, ApJ, 473, 88
Riess, A. G., et al. 1998, AJ, 116, 1009
Riess, A. G., et al. 1999, AJ, 117, 707
Riess, A. G., et al. 2004, ApJ, 607, 665
Riess, A. G., et al. 2007, ApJ, 659, 98
Riess, A. G., et al. 2009, ApJ, 699, 539
Sasaki, M. 1987, MNRAS, 228, 653
Schlegel, D. J., Finkbeiner, D. P., & Davis, M. 1998, ApJ, 500, 525
Schmidt, B. P., et al. 1998, ApJ, 507, 46
Sheinis, A. I., Bolte, M., Epps, H. W., Kibrick, R. I., Miller, J. S., Radovan, M. V., Bigelow, B. C., & Sutin, B. M. 2002, PASP, 114, 851
Simon, J. D., et al. 2009, ApJ, 702, 1157
Stetson, P. B. 2000, PASP, 112, 925
Stritzinger, M., Suntzeff, N. B., Hamuy, M., Challis, P., Demarco, R., Germany, L., & Soderberg, A. M. 2005, PASP, 117, 810
Strovink, M. 2007, ApJ, 671, 1084
Thatte, D., et al. 2009, NICMOS Data Handbook (ver. 8.0; Baltimore, MD: STScI)
Tonry, J. L., et al. 2003, ApJ, 594, 1
Tripp, R. 1998, A&A, 331, 815
Wang, L. 2005, ApJ, 635, L33
Wang, L., Goldhaber, G., Aldering, G., & Perlmutter, S. 2003, ApJ, 590, 944
Wang, X., et al. 2008, ApJ, 675, 626
Wood-Vasey, W. M., et al. 2007, ApJ, 666, 694